

# Lawrence Berkeley National Laboratory

## LBL Publications

### Title

WHITE DWARF MERGERS ON ADAPTIVE MESHES. I. METHODOLOGY AND CODE VERIFICATION

### Permalink

<https://escholarship.org/uc/item/8x60n0ks>

### Journal

The Astrophysical Journal, 819(2)

### ISSN

0004-637X

### Authors

Katz, Max P  
Zingale, Michael  
Calder, Alan C  
[et al.](#)

### Publication Date

2016-03-10

### DOI

10.3847/0004-637x/819/2/94

Peer reviewed

# WHITE DWARF MERGERS ON ADAPTIVE MESHES I. METHODOLOGY AND CODE VERIFICATION

MAX P. KATZ<sup>1</sup>, MICHAEL ZINGALE<sup>1</sup>, ALAN C. CALDER<sup>1,2</sup>, F. DOUGLAS SWESTY<sup>1</sup>, ANN S. ALMGREN<sup>3</sup>, AND WEIQUN ZHANG<sup>3</sup>

<sup>1</sup> Department of Physics and Astronomy, Stony Brook University, Stony Brook, NY, 11794-3800, USA

<sup>2</sup> Institute for Advanced Computational Sciences, Stony Brook University, Stony Brook, NY, 11794-5250, USA

<sup>3</sup> Center for Computational Sciences and Engineering, Lawrence Berkeley National Laboratory, Berkeley, CA 94720

## ABSTRACT

The Type Ia supernova progenitor problem is one of the most perplexing and exciting problems in astrophysics, requiring detailed numerical modeling to complement observations of these explosions. One possible progenitor that has merited recent theoretical attention is the white dwarf merger scenario, which has the potential to naturally explain many of the observed characteristics of Type Ia supernovae. To date there have been relatively few self-consistent simulations of merging white dwarf systems using mesh-based hydrodynamics. This is the first paper in a series describing simulations of these systems using a hydrodynamics code with adaptive mesh refinement. In this paper we describe our numerical methodology and discuss our implementation in the compressible hydrodynamics code CASTRO, which solves the Euler equations, and the Poisson equation for self-gravity, and couples the gravitational and rotation forces to the hydrodynamics. Standard techniques for coupling gravitation and rotation forces to the hydrodynamics do not adequately conserve the total energy of the system for our problem, but recent advances in the literature allow progress and we discuss our implementation here. We present a set of test problems demonstrating the extent to which our software sufficiently models a system where large amounts of mass are advected on the computational domain over long timescales. Future papers in this series will describe our treatment of the initial conditions of these systems and will examine the early phases of the merger to determine its viability for triggering a thermonuclear detonation.

*Keywords:* hydrodynamics - methods: numerical - supernovae: general - white dwarfs

## 1. INTRODUCTION

Type Ia supernovae (SNe Ia) are among the most exciting events to study in astrophysics. These bright, brief pulses of light in the distant universe have led to a number of important discoveries in recent years, including the discovery of the accelerated expansion of the universe (Perlmutter et al. 1999; Riess et al. 1998). Their origin, though, is shrouded in mystery. It has long been expected that these events arise from the thermonuclear explosions of white dwarfs (Hoyle & Fowler 1960), but the cause of these explosions is uncertain. In particular, it is not clear what process causes the temperatures in these white dwarfs (WDs) to become hot enough for explosive burning of their constituent nuclei. The model favored initially by the community was the single-degenerate (SD) model (Whelan & Iben 1973). Accretion of material from a companion star such as a red giant would cause the star to approach the Chandrasekhar mass, and in doing so the temperature and density in the center would become sufficient for thermonuclear fusion to proceed. In recent years the focus has shifted

to a number of alternative progenitor models. A leading candidate for explaining at least some of these explosions is the double-degenerate (DD) model, in which two white dwarfs merge and the merged object reaches the conditions necessary for a thermonuclear ignition (Iben & Tutukov 1984; Webbink 1984). Another is the double detonation scenario, where accretion of material onto a sub-Chandrasekhar mass white dwarf leads to a detonation inside the accreted envelope, sending a compressional wave into the core of the star that triggers a secondary detonation. A recent review of the progenitor models can be found in Hillebrandt et al. (2013).

There are several observational reasons why double-degenerate systems are a promising progenitor model for at least a substantial fraction of normal SNe Ia. No conclusive evidence exists for a surviving companion star of a SN Ia; this is naturally explained by the DD model because both WDs are likely to be destroyed in the merger process. Similarly, pre-explosion images of the SN Ia systems have never clearly turned up a companion star, and in some cases a large fraction of the parameter space

for the nature of the companion star is excluded. Additionally, not enough progenitor systems are seen for the SD case to match the observed local SN Ia rate, whereas the number of white dwarf binaries may be sufficient to account for this rate. Finally, the DD model can naturally explain the fact that many SNe Ia are observed to occur at very long delay times after the stars were formed, since the progenitor systems only become active once both stars have evolved off the main sequence. A thorough review of the observational evidence about SNe Ia and further discussion of these ideas can be found in [Maoz et al. \(2014\)](#).

The first attempts to model the results of the merger process came in the 1980s. [Nomoto & Iben \(1985\)](#) demonstrated that off-center carbon ignition would occur in the more massive white dwarf as it accreted mass near the Eddington rate from the less massive white dwarf overflowing its Roche lobe. [Saio & Nomoto \(1985\)](#) tracked the evolution of the flame and found that it propagated quiescently into the center, converting the carbon-oxygen white dwarf into an oxygen-neon-magnesium white dwarf. This would then be followed by collapse into a neutron star—a result with significantly different observational properties compared to a SN Ia. This scenario, termed accretion-induced collapse, would be avoided only if the accretion rate were well below the Eddington rate (see, e.g., [Fryer et al. \(1999\)](#) for a discussion of the possible implications of the accretion-induced collapse scenario). [Tutukov & Yungelson \(1979\)](#) observed that the collapse could be avoided if the mass loss from the secondary was higher than the Eddington rate and thus the accreted material formed an accretion disc, which might rain down on the primary more slowly. The main finding was that double degenerate systems would not obviously lead to Type Ia supernovae.

Three-dimensional simulations of merging double degenerate systems were first performed by [Benz et al. \(1990\)](#), who used the smoothed particle hydrodynamics (SPH) method to simulate the merger process. This was followed later by a number of authors ([Rasio & Shapiro 1995](#); [Segretain et al. 1997](#); [Guerrero et al. 2004](#); [Yoon et al. 2007](#); [Lorén-Aguilar et al. 2009](#); [Raskin et al. 2012](#)). The main finding of these early 3D SPH simulations was that if the lower-mass star (generally called the “secondary”) was close enough to the more massive star (the “primary”) to begin mass transfer on a dynamical time scale, the secondary completely disrupted and formed a hot envelope around the primary, with a centrifugally-supported accretion disk surrounding the core and envelope. Carbon fusion might commence in the disk, but not at a high enough rate to generate a nuclear detonation. [Mochkovitch & Livio \(1990\)](#) and [Livio \(2000\)](#) also observed that turbulent viscosity in this disk would be sufficiently large for

angular momentum to be removed from the disk at a rate high enough to generate the troublesome accretion timescales discussed by [Tutukov & Yungelson \(1979\)](#) and mentioned above. Based on this evidence, the review of [Hillebrandt & Niemeyer \(2000\)](#) argued that the model was only viable if the accretion-induced collapse problem could be avoided. Later work by [Shen et al. \(2012\)](#) and [Schwab et al. \(2012\)](#) used a more detailed treatment of the viscous transport in the outer regions of the remnant and found that viscous dissipation in the centrifugally supported envelope would substantially heat up the envelope on a viscous timescale, but their simulations still led to off-center carbon burning. [van Kerkwijk et al. \(2010\)](#) argued that equal-mass mergers would lead to the conditions necessary for carbon detonation in the center of the merged object, but [Shen et al. \(2012\)](#) also questioned this for reasons related to how viscous transport would convert rotational motion into pressure support. [Zhu et al. \(2013\)](#) followed this with an expanded parameter space study and argued that many of their carbon-oxygen systems had the potential to detonate. The study of the long-term evolution of the remnants is thus still an open subject of research.

A recent shift in perspective on this problem started around 2010. [Pakmor et al. \(2010\)](#) used the SPH method to study the merger of equal-mass ( $0.9 M_{\odot}$ ) carbon-oxygen white dwarfs and found that a hotspot was generated near the surface of the primary white dwarf. They argued that this region had a temperature and density sufficient to trigger a thermonuclear detonation. They inserted a detonation which propagated throughout the system. They found that the result would observationally appear as a subluminous Type Ia supernova. This was the first time a DD simulation successfully reproduced at least some characteristics of a SN Ia. [Pakmor et al. \(2011\)](#) tried a few different mass combinations and found empirically that this would hold as long as the secondary was at least 80% as massive as the primary. These events, where the merger process resulted in the detonation of the system during the merger coalescence—avoiding the much longer time-scale evolution—were termed “violent” mergers.

Around the same time, however, [Guillochon et al. \(2010\)](#) and [Dan et al. \(2011\)](#) pointed out that the previously mentioned simulations generally shared a significant drawback, which was that their initial conditions were not carefully constructed. [Motl et al. \(2002\)](#), [D’Souza et al. \(2006\)](#), and [Motl et al. \(2007\)](#) (the first three-dimensional mesh-based simulations of mass transfer in binary white dwarf systems) pioneered the study of the long-term dynamical evolution of binary white dwarf systems after constructing equilibrium initial conditions. Earlier work placed the stars too close together and ig-

nored the effects of tidal forces that change the shape of the secondary, leading to the merger happening artificially too quickly (Fryer & Diehl 2008). When the initial conditions are constructed in equilibrium, the system can be stable for tens of orbital periods, substantially changing the character of the mass transfer phase. One limitation of this series of studies is that the authors used a polytropic equation of state and thus could not consider nuclear reactions. Guillochon et al. (2010) and Dan et al. (2011) improved on this using a realistic equation of state, a nuclear reaction network, and a similar approach to the equilibrium initial conditions, and found substantial agreement with the idea that mass transfer occurs in a stable manner over tens of orbital periods. They also found that, assuming the material accreted onto the surface of the primary was primarily helium, explosive surface detonations would occur as a result of accretion stream instabilities during the mass transfer phase prior to the full merger. This could trigger a double-detonation explosion and thus perhaps a SNe Ia.

The latest violent merger developments have resulted in some possible areas of convergence. Pakmor et al. (2012b) performed a merger scenario with a  $1.1 M_{\odot}$  and  $0.9 M_{\odot}$  setup, with better treatment of the initial conditions, and indeed found that the merger process happened over more than ten orbits. Nevertheless, they still determined that a carbon-oxygen detonation would occur, in line with their earlier results. Moll et al. (2014) and Kashyap et al. (2015) were also able to find a detonation in similarly massive systems. Notably, the detonation occurred self-consistently and did not need to be intentionally triggered using an external source term. Dan et al. (2012) and Dan et al. (2014) performed a large sweep of the parameter space for merger pairs and found that pure carbon-oxygen systems would generally not lead to detonations (and thus be violent mergers) except for the most massive systems. They did find that for systems with WDs containing helium, many would detonate and potentially lead to SNe Ia, either through the aforementioned instabilities in the accretion stream, or during the contact phase, similar to the violent carbon-oxygen WD mergers. Sato et al. (2015) also examined the parameter space and came to a similar conclusion for massive carbon-oxygen WD systems (and also looked at the possibility of detonations after the coalescence had completed), while Tanikawa et al. (2015) discussed the plausibility of helium detonations in the massive binary case. Pakmor et al. (2013) added a thin helium shell on their primary white dwarf, and found that this robustly led to a detonation of the white dwarf. For now there is preliminary support for the hypothesis that systems with helium shells (or helium WDs), and very massive carbon-oxygen binaries, could robustly lead to events resembling

SNe Ia.

Given the considerable research into the double degenerate problem described above, why is another approach using a different simulation code warranted? First and foremost, reproducibility of the results across simulation codes and algorithms is important for gauging confidence in this result. Most of the existing results that study the viability of double degenerate systems as progenitors for Type Ia supernovae (that is, including a realistic equation of state and nuclear reactions) have used the SPH method. SPH codes have a number of features which do aid them in the study of these systems, such as conservation of angular momentum to machine precision when there are no source terms such as gravity (and conservation proportional to the level of tolerance of error in the gravity solver when gravity is used). A drawback relates to the fact that whether a prompt detonation in a merger happens depends in detail on the nature of the gas at the interface between the two stars, which is at much lower density than the rest of the stellar material. The SPH codes for these simulations generally all use uniform mass particles, so their effective resolution is *lowest* at the stellar surface. In contrast, a code with adaptive mesh refinement can zoom in on the regions where hotspots will develop, while also maintaining high enough resolution in the high-density regions to adequately capture the large-scale mass transfer dynamics. There are also outstanding questions of convergence in SPH (e.g. Zhu et al. 2014) and whether the method correctly captures fluid instabilities. This is an important question for white dwarf mergers because of the likely importance small-scale instabilities will have on the evolution of the low-density gas at the primary’s surface. The pioneering work of Agertz et al. (2007) compared grid and SPH codes and found some important differences. Most relevant for this discussion is that the SPH codes could not adequately handle mixing from the Kelvin-Helmholtz instability in the test they propose. As pointed out by Price (2008), this is not a result of SPH being inherently unable to model this instability, but instead it is attributed to the fact that the standard SPH evolution equations do not have a mechanism for capturing discontinuities in internal energy. Price showed that the addition of an artificial thermal conductivity can dramatically improve the ability of the SPH codes to exhibit this instability. There have since been a number of other papers discussing this issue, but to our knowledge none of these improvements have yet been incorporated into an SPH model of a WD merger. Another reason for caution is that other than the most recent results of Kashyap et al. (2015), no white dwarf merger simulation has self-consistently resulted in a thermonuclear detonation. Reproducibility of the detonation through numerical simulation is critical for building confidence in this progenitor model.

This paper is the first in a series designed to address these outstanding theoretical issues for white dwarf mergers. This work discusses the verification of our hydrodynamics code for simulating these events. Later efforts will look at the initial conditions of the system, the robustness with which a hotspot is found from which a detonation could occur, and the importance of the initial white dwarf models, which should be more sophisticated than simple carbon-oxygen mixtures and in principle should use results from modern stellar evolution calculations. [Section 2](#) describes our code and why it can provide useful results compared to other methodologies used for this problem. [Section 3](#) describes the method we use for setting up a binary white dwarf simulation. [Section 4](#) discusses a few test problems that we use to verify that our code accurately solves the equations of fluid dynamics. [Section 5](#) demonstrates that the software scales well for supercomputer applications. Finally, [Section 6](#) recaps what we have shown and highlights some of the future work we plan to do.

## 2. NUMERICAL METHODOLOGY

To study the white dwarf merger problem, we use the mesh-based hydrodynamics code `CASTRO`<sup>1</sup> ([Almgren et al. 2010](#)). `CASTRO` solves the Euler equations, along with the inclusion of optional modules for gravity, nuclear reactions and thermodynamics. `CASTRO` is based on the `BoxLib`<sup>2</sup> adaptive-mesh refinement (AMR) framework ([Rendleman et al. 2000](#)), which represents fluid data on a hierarchical mesh where regions of interest have higher spatial resolution. `CASTRO` is highly parallel and is designed for large-scale use on modern supercomputers; see [Section 5](#) for information on how `CASTRO` performs for our problem. The next few subsections describe our approach to each of the physics components used in this work. We direct the reader to the original code paper for a full description of `CASTRO`'s approach to solving the equations of hydrodynamics. In this work, we report mainly on the changes we have made to the code since its original release, for the purpose of approaching this problem.

### 2.1. Hydrodynamics

The Euler equations for hydrodynamics (in the absence of source terms) in conservative form are:

$$\frac{\partial \rho}{\partial t} = -\nabla \cdot (\rho \mathbf{u}) \quad (1)$$

$$\frac{\partial \rho \mathbf{u}}{\partial t} = -\nabla \cdot (\rho \mathbf{u} \mathbf{u}) - \nabla p \quad (2)$$

$$\frac{\partial \rho E}{\partial t} = -\nabla \cdot (\rho \mathbf{u} E + p \mathbf{u}). \quad (3)$$

Here  $\rho$  is the mass density,  $\mathbf{u} = (u, v, w)$  is the fluid velocity vector,  $p$  is the pressure, and  $E = \mathbf{u}^2/2 + e$  is the total specific energy, where  $e$  is the internal (thermal) specific energy (energy per unit mass).

We use the unsplit piecewise-parabolic method (PPM) solver in `CASTRO` to advance the hydrodynamics system in time ([Miller & Colella 2002](#)). A number of changes were made to the solver, which are detailed in [Appendix A](#). These changes bring the algorithm more in line with that of [Colella & Woodward \(1984\)](#). `CASTRO` as originally released featured a slightly modified version of the higher resolution limiters of [Colella & Sekora \(2008\)](#), which can be used in the code by setting `castro.ppm_type = 2` in the inputs file (the inputs file is a set of code parameters accessed at runtime to determine the algorithms used in the simulation). The advantage of this limiter is that it preserves physical extrema rather than clipping them off as in the original approach of [Colella & Woodward \(1984\)](#). Despite the advantages of this limiter we have found it to be unsatisfactory for our problem. There are many regions in our problem with large density gradients (such as the interface between the star's atmosphere and the ambient gas outside of it) and in these regions the algorithm can yield negative densities. This often results from the limiters interpreting these gradients as being true minima. As a result, we use the original limiter, which is strictly monotonicity preserving in the parabolic profiles it generates; this is activated with `castro.ppm_type = 1` in the inputs file.

A related issue that required a code improvement is that in cases of large density gradients such as the edge of a star, it is possible to generate negative densities in zones even with the more strongly limited PPM. This can occur if a region of large density is moving away from an ambient zone at relatively large speeds; then the net density flux in the ambient zones can be large enough to unphysically drag the density below zero. In practice, this occurs at the trailing edge of a star that is moving across a grid. In such a situation, there are two main approaches one could take: either explicitly introduce a positivity-guaranteeing diffusive flux, or reset the properties of the affected zone. We choose the latter approach. Even though it is non-conservative, it preserves a characteristic we value, which is to keep the edge of the stars relatively sharp, as they physically should be.

<sup>1</sup> `CASTRO` can be obtained at <https://github.com/BoxLib-Codes/Castro>.  
<sup>2</sup> `BoxLib` can be obtained at <https://github.com/BoxLib-Codes/BoxLib>.

Since the mass of the affected zones is typically already fairly low, this should not seriously affect the dynamics or the energy conservation properties of our simulation. Our strategy for a reset is as follows: when the density of a zone is below a pre-determined density floor (which is typically  $10^{-5} \text{ g cm}^{-3}$  for our stellar simulations), we look at all adjacent zones and find the zone with the highest density. If it is above the density floor, then we set the field values (density, momentum, energy, and temperature) of the reset zone to be equal to the field values of this adjacent zone. If no adjacent zone reaches the density floor, then the zone is set to the density floor, and given a temperature equal to the temperature floor for our simulations (which is typically  $10^5 \text{ K}$  for our stellar simulations). We then recompute the thermodynamics to be consistent with these values. The velocity of the zone is set to zero. This latter approach only occurs in very rare situations, and is there as a last resort.

CASTRO’s approach to adaptive mesh refinement, based on its underlying `BoxLib` framework, is to refine zones based on certain user-specified criteria that tag regions of interest for higher spatial resolution. Data is represented on one of a number of AMR levels, where each level corresponds to a set of zones at the same resolution, which covers a subset of the domain covered by the level immediately below it. We typically call the level 0 grid the *coarse* grid, which has the lowest spatial resolution. Each finer, higher-level grid has a higher resolution than the grid below it by some integer factor  $N$ , which is restricted to be  $N = 2$  or  $4$  in CASTRO. The zones are strictly contained within the rectangular extent of the underlying coarser zones (at present, in 3D the code is restricted to representing only Cartesian geometries with uniform spacing in each dimension). For the time evolution of the AMR system we use subcycling, where each AMR level is advanced at a different timestep and a correction step is applied at the end to synchronize the various levels. The number of subcycled timesteps is equal to the jump in refinement between levels, so for example on a grid with three levels and two jumps of four in refinement, the level 2 zones have 16 times higher spatial resolution than the coarse grid and there are 16 level 2 timesteps per level 0 timestep.

The boundary conditions on the hyperbolic system are simply zero-gradient zones that allow material to flow directly out of the domain. Using AMR, we make the coarse grid large enough that the boundaries are relatively far from the region of interest. This ensures that any boundary effects do not pollute the inner region where the stars will eventually make contact. We further make the restriction that refined grids cannot reach the domain boundary.

## 2.2. Microphysics

The equation of state (EOS) for our simulations is the Helmholtz EOS (Timmes & Swesty 2000). This models an electron-positron gas of arbitrary relativity and degeneracy over a wide range of temperatures and densities. Thermodynamic quantities are calculated as derivatives of the Helmholtz free energy, and the values are interpolated from a table. The natural variables of the Helmholtz free energy are temperature and density, and calling the EOS is simplest in this form. In hydrodynamics we often have the density and internal energy as independent variables, and we want to obtain the temperature, pressure, and other quantities. To do this, we employ a Newton-Raphson iteration over the temperature (given some sufficient starting guess) until we find the temperature that corresponds to the desired internal energy. Sometimes this process fails to converge and the iterative value approaches zero. In these cases we employ a “floor” that limits how low the temperature can go (typically  $10^5 \text{ K}$ ). There is a choice here how to proceed: we can either assign this floor value to the temperature and let that zone be thermodynamically inconsistent (the original behavior in CASTRO), or we can adjust the internal energy to be thermodynamically consistent with the temperature, at the cost of violating energy conservation. We have found in some test problems of strong one-dimensional shocks that reach the temperature floor that the latter yields more accurate results. However, allowing the equation of state call to update the internal energy can actually result in significant changes to the total energy of the system over long periods of time, due not just to resets in low-density zones but also to small inconsistencies between the energy given to the EOS and the energy that is consistent with the returned temperature. These inconsistencies are dependent on the tolerance of the Newton-Raphson iterative solve. While this error tolerance is typically very small in an individual zone (a relative difference of  $10^{-8}$  by default in CASTRO), over time and given a large number of zones, this can result in a significant energy drift. This is a serious enough problem that we opt for the energy conserving approach for our simulations.

CASTRO has the ability to model both nuclear reactions and radiative transport (in the flux-limited diffusion approximation). For all simulations in this paper we do not enable either, and we delay discussion of these modules until later papers in this series.

## 2.3. Gravity

We solve the Poisson equation for self-gravity for our problem,

$$\nabla^2 \Phi(\mathbf{x}) = 4\pi G \rho(\mathbf{x}), \quad (4)$$

where  $\Phi$  is the gravitational potential,  $G$  is the gravitational constant, and  $\rho$  is the mass density.<sup>3</sup> The solution of this equation in *CASTRO* is described in [Almgren et al. \(2010\)](#), and consists of both level and composite solves, and (optionally) a final synchronization at the end. We do not enable this final synchronization for the merger simulations, because the grid boundaries never lie in regions of high density, so the change in the potential due to the correction at coarse–fine interface is always negligible.

### 2.3.1. Coupling to Hydrodynamics

The effect of gravity on the hydrodynamical evolution is typically incorporated by the use of a source term for the momentum and energy equations. In a finite volume methodology, the momentum source term often appears in integral form as

$$\left. \frac{\partial(\rho \mathbf{u})}{\partial t} \right|_{\text{grav}} = \frac{1}{\Delta V} \int \rho \mathbf{g} dV \quad (5)$$

and for the energy source term it is

$$\left. \frac{\partial(\rho E)}{\partial t} \right|_{\text{grav}} = \frac{1}{\Delta V} \int \rho \mathbf{u} \cdot \mathbf{g} dV. \quad (6)$$

Here  $\Delta V$  is the cell’s volume. In most hydrodynamics codes these are discretized as  $\rho \mathbf{g}$  and  $\rho \mathbf{u} \cdot \mathbf{g}$ , respectively, where  $\rho$ ,  $\mathbf{u}$ , and  $\mathbf{g}$  are evaluated at the zone center.

There are two ways that these source terms enter the system evolution. First, during the hydrodynamics update, we alter the edge states that enter into the determination of the fluxes. (This only applies for the momentum source term; the gravitational force does not directly do work on the internal energy, which is used to infer the pressure.) To second order in space and time, this can be done using the cell-centered source term evaluated at time-level  $n$ . We choose a more accurate approach, which is also second order, of characteristic tracing under the source term; the details of this are described in [Appendix A](#). Second, after the hydrodynamics step, we add the time-centered source terms to the state. First we describe how we do this for the momentum, and then we describe our approach for the energy. This discussion is somewhat detailed. We believe that the attention is necessary because of the importance of accuracy in the gravitational source terms for our problem. The stability of the white dwarf binary system is dependent in large part upon accurate coupling of the hydrodynamics and gravity; an error in this approach could lead to, for example, a spurious mass transfer episode that might lead us to very different conclusions about the long term stability of such a system. Such considerations are generally

<sup>3</sup> In the *CASTRO* code, the right-hand side is negated and therefore  $\Phi$  is positive. We use the sign convention that is typical for astrophysics in this paper. When  $\Phi$  appears in the code it is negated to compensate for this.

unimportant for spherically-symmetric single star calculations, but are of the utmost importance in a simulation where the global gravitational field can change quite significantly over the course of the simulation.

In a system with self-gravity, total momentum is conserved if the spatial domain includes all of the mass of the system. This must be the case because each mass element exerts an equal and opposite gravitational force on every other mass element. However, the standard approach does not necessarily guarantee that momentum is conserved numerically. We cannot represent a vacuum state in our code, so there is a small but non-zero density on the edge of the grid. This allows momentum to leak out of the domain even if the gravitational source term is written in an explicitly conservative manner. To see this, one can use the Poisson equation to write the density in terms of the potential and then consider its spatial discretization. For simplicity, we consider one spatial dimension and a uniform discretization. Analogous results may be readily obtained for the non-uniform case.

$$\begin{aligned} -\rho_i \frac{d\Phi_i}{dx} &= -\frac{1}{4\pi G} \frac{d^2\Phi_i}{dx^2} \frac{d\Phi_i}{dx} \\ &= -\frac{1}{4\pi G} \left[ \frac{\Phi_{i-1} - 2\Phi_i + \Phi_{i+1}}{\Delta x^2} \right] \left[ \frac{\Phi_{i+1} - \Phi_{i-1}}{2\Delta x} \right] \\ &= -\frac{1}{8\pi G \Delta x^3} [\Phi_{i+1}^2 - \Phi_{i-1}^2 - 2\Phi_i(\Phi_{i+1} - \Phi_{i-1})] \end{aligned} \quad (7)$$

It is easy to verify that adding the source terms for the current zone and the two zones to the left and right results in complete cancellation of the source terms. The catch is that if the potential is non-zero outside of the domain, then there will be momentum lost or gained from the grid, which will be encapsulated in the ghost cells just outside the domain. In addition, when we replace the Laplacian above by the full three-dimensional stencil including the  $y$  and  $z$  derivatives, depending on the discretization these may not be cancelled at all. This latter problem can be resolved by writing the momentum update in an explicitly conservative way.

[Shu \(1992, Chapter 4\)](#) observes that it is possible to describe the source term for the momentum equation by taking the divergence of a gravitational stress tensor,

$$G_{ij} = -\frac{1}{4\pi G} \left( g_i g_j - \frac{1}{2} |\mathbf{g}|^2 \delta_{ij} \right). \quad (8)$$

The momentum equations are then written explicitly in conservative form. The flux at any zone boundary is added to one cell and subtracted from another, so that the total momentum in the domain interior stays constant to within numerical roundoff error. This result can be derived by analytically recasting [Equation 7](#). In the continuum limit, the two momentum formulations are identical. Thus the latter has been advocated by, for

example, [Jiang et al. \(2013\)](#) for the ATHENA code. A significant limitation to this approach is that in a finite discretization the divergence of the gravitational acceleration is no longer guaranteed to equal the zone density. In particular, we find that the mixing of the gravitational acceleration components means that the truncation error in the gravitational field can lead to large errors that imply a density much different than the zone’s actual density. This is especially problematic in a simulation with a low-density ambient medium, where even a small error in the momentum update can lead to large changes in a zone’s momentum. By continuing to explicitly use the cell density in the momentum update, we can avoid this possibility: the size of the update will always be suitably small if the zone’s density is small. Thus for our simulations we continue to use the standard source term for the momentum.

Time centering of this source term is done in **CASTRO** using a predictor-corrector approach. At the start of a coarse grid timestep, we solve the gravitational potential for the density  $\rho^n$ . We then add to the momenta a prediction of the source term that is first-order accurate in time,  $\Delta t \rho^n \mathbf{g}^n$ . After the hydrodynamics update, we recalculate the gravitational potential based on the new density,  $\rho^{n+1}$ , and then add  $-(\Delta t/2)\rho^n \mathbf{g}^n + (\Delta t/2)\rho^{n+1} \mathbf{g}^{n+1}$  to the momenta.

For the energy equation, the central challenge is to write down a form of the discretized energy equation that explicitly conserves total energy when coupled to gravity. When gravity is included, the conserved total energy over the entire domain is

$$\int \rho E_{\text{tot}} dV = \int dV \left( \rho E + \frac{1}{2} \rho \Phi \right), \quad (9)$$

where  $\rho E$  is the total gas energy from the pure hydrodynamics equation. The factor of 1/2 in the gravitational energy is necessary for simulations with self-gravity to prevent double-counting of interactions (since in dynamical evolution the relevant gravitational potential energy is  $\rho \Phi$  and the gravitational force is  $\rho \mathbf{g}$ ). Historically many simulation codes with gravity have not used a conservative formulation of the energy equation, but it is straightforward to do so. Our approach, and the discussion that follows, is based on that of [Springel \(2010\)](#).

Conservation of total energy requires that a change in gravitational energy is compensated for by a change in gas energy, and that energy changes due to mass transfer are explicitly and exactly tracked. Suppose that we have some fluid mass  $\Delta M_{i+1/2} = \Delta \rho_{i+1/2} \Delta V$  leave the zone with index  $i$  and enter the zone with index  $i + 1$ . The subscript indicates that the mass change is occurring at the interface between the two zones, at index  $i + 1/2$ . The work done by the gravitational force on the gas is  $\Delta(\rho E) = W = \int F dx = (\Delta M_{i+1/2} g_{i+1/2})(\Delta x/2)$ ,

where  $g_{i+1/2}$  is the gravitational acceleration at the interface. The second term in parentheses is just the distance from the zone center to the zone edge: once the mass leaves the zone edge, it no longer needs to be tracked. To second order,  $g_{i+1/2} = -(\Phi_{i+1} - \Phi_i)/\Delta x$ , and also to second order the potential at the interface is given by  $\Phi_{i+1/2} = (\Phi_{i+1} + \Phi_i)/2$ , so we can equivalently view the work done as  $W = -\Delta M_{i+1/2}(\Phi_{i+1/2} - \Phi_i)$ . Physically, this is just the negative of the gravitational potential energy change as the fluid is pushed from the cell center potential to the cell edge potential, exactly as the work-energy theorem implies.

Now, in a hydrodynamics code, mass changes correspond to hydrodynamic fluxes. In particular, the continuity equation tells us that the mass flux  $F_\rho = \rho_{i+1/2}^{n+1/2} v_{i+1/2}^{n+1/2}$  yields an integrated mass motion through the interface  $i + 1/2$  over a timestep  $\Delta t$  of:

$$\Delta \rho_{i+1/2} = \frac{\Delta t}{\Delta V} \left( \rho_{i+1/2}^{n+1/2} v_{i+1/2}^{n+1/2} dA \right). \quad (10)$$

Note that here  $v_{i+1/2}$  is the component of the velocity perpendicular to the zone face, whose area is  $dA$ .

Finally, then, we write the update in a zone for the total energy that conserves  $(\rho E_{\text{tot}})$  as:

$$\Delta(\rho E) = -\frac{1}{2} \sum_f \Delta \rho_f (\Phi_{f+1/2} - \Phi_{f-1/2}), \quad (11)$$

where the sum is over the cell faces with indices  $f$  and the indices  $f + 1/2$  and  $f - 1/2$  refer to the zone centers immediately to the left and right in the direction perpendicular to the face. As long as we record the hydrodynamical fluxes through the zone faces after coming out of the hydrodynamics step, this algorithm is able to conserve the total energy completely (except for any energy loss or gain through physical domain boundaries). In order for the method to be second-order accurate in time, we need to use a time-centered  $\Phi$  (which can be computed by averaging the time-level  $n$  and  $n + 1$  potentials; we already have the latter because **CASTRO** re-computes the potential at the new time after the hydrodynamics step, and we can apply this energy at the end of the timestep). Note that of course the hydrodynamical flux is already second-order accurate in time. We observe also that in practice we will not obtain conservation of energy to machine precision even in the absence of open domain boundaries. The method itself is conservative if it is time-centered and correctly evaluates the energy change on cell faces. This was demonstrated empirically by [Jiang et al. \(2013\)](#) and is obvious in the case of a fixed external potential; it is not as obvious in the case of the gravitational self-potential, which changes in response to changes in the mass distribution, so we give a short proof of this in [Appendix B](#). However, in practice there is a non-zero numerical tolerance associated with the Poisson



gravity solver (in our case, the multigrid method) that results in a non-zero error in the calculation of the gravitational potential. This results in a very small deviation from perfect conservation. It is not usually larger than the other effects which result in energy non-conservation for our simulations, such as resetting the state of zones that acquire a negative internal energy, and in principle if desired it can be made smaller by using stricter tolerance levels on the gravity solve.

In passing, we hope to clear up a spot of potential confusion, that we feel is unclear in other papers on this subject: the factor of 1/2 that appears in Equation 11 has nothing to do with the factor of 1/2 that appears in the statement of conservation of total energy, Equation 9. The former comes simply from the fact that the energy change is evaluated using the mass motion through a distance of half of the zone width. The latter is needed to ensure that these local changes in energy are not double-counted when doing a global integral, since the gravitational potential is self-generated. Equation 11 applies to any conservative potential  $\Phi$ , and we use this to our advantage for the rotation forces in Section 2.4.

As observed by Springel (2010), this method is more accurate than the more common (non-conservative) approach of evaluating the change in gas energy using the work done ( $\mathbf{v} \cdot \rho \mathbf{g}$ ) by the gravitational force at the cell center. Analytically this form expresses the same core idea as Equation 11 via the work-energy theorem, but a major flaw is that it evaluates the energy change at the cell center when in fact the mass transfer is happening at the cell edges. This can result in a significant leaking of energy throughout the course of the evolution, dramatically affecting the course of the evolution. The standard approach is therefore unacceptable in the case of a problem like white dwarf mergers, and the fix to this energy leaking—evaluating the energy transfer at the six zone faces instead of the single zone center—adds only a very minor cost in terms of code complexity and computational time.

Another approach to conserving total energy recently taken in the literature is to evolve an equation for the total energy ( $\rho E_{\text{tot}}$ ); see Jiang et al. (2013) (see also Springel (2010), Section 5.3). That is, one can replace the gas energy equation with a total energy equation, and then the energy flux includes a term corresponding to the flux of gravitational potential energy. We avoid this approach for our problem because there are regions on the computational domain where the total energy is dominated by potential energy (especially the low-density regions near the edge of the white dwarfs), and the gas energy can only be retrieved by first subtracting  $-\rho\Phi/2$  from the total energy. Like Springel (2010), we find that this can result in some serious errors due to numerical discretization, yielding unphysical energies

or temperatures. We observe also that the implementation of Jiang et al. (2013) has terms in the gravitational flux that are not proportional to  $\rho$ , and so can lead to the same troubles that plague the tensor-based formalism for the momentum equation, where small errors in the discretization of the gravitational potential can lead to very large changes in the energy of the gas.

### 2.3.2. Boundary Conditions

Analytical solutions to the Poisson equation customarily assume that the potential vanishes at large distances from the region of non-zero density. On a finite computational domain, however, it is usually not possible to have the edges of the domain be far enough away that the potential can be taken to be zero there. Solving the Poisson equation therefore requires knowledge of the values of the potential on the edges of the computational domain. In principle, the boundary values can be computed by doing a direct sum over the mass distribution inside the domain, where the mass in each zone is treated as a point source:

$$\Phi_{lmn} = - \sum_{i,j,k} \frac{G\rho_{ijk}}{|\mathbf{x}_{lmn} - \mathbf{x}_{ijk}|} \Delta V_{ijk}. \quad (12)$$

Here  $(i, j, k)$  are the indices of cells inside the domain, and  $(l, m, n)$  are the indices of ghost zones outside the domain where the boundary values for the potential is specified<sup>4</sup>.  $\Delta V$  is the volume of the zone. If there are  $N$  zones per spatial dimension, then there are  $6N^2$  boundary zones, and each boundary zone requires a sum over  $N^3$  zones, so the direct computation of the boundary conditions scales as  $\mathcal{O}(N^5)$ . This method is expensive enough that it is not used for hydrodynamics simulations (though it is useful for comparison to approximate solutions, so we have implemented it as an option in CASTRO).

In a typical simulation we place the boundaries of the domain far enough away from the region containing most of the mass that some method of approximation to this direct summation is justified. Many approaches exist in the literature. The original release of CASTRO featured the crudest possible approximation: a monopole prescription, where the boundary values were computed by summing up all the mass on the domain and treating it as a point source at the domain center. This is correct only for a spherically symmetric mass distribution, and therefore is best suited for problems like single-star Type Ia supernova simulations (e.g. Malone et al. (2014)) that employ self-gravity. For a problem like that of a binary star system with significant departures from spherical symmetry, this assumption fails to produce accurate boundary values, which we find in Section 4.4 re-

<sup>4</sup> In CASTRO we actually specify the potential on cell edges, not on cell centers, but the idea is the same, and we use the location of the cell edge in computing the distance to each zone in the domain.

sults in a significant drift of the center of the mass of the system over time.

The most natural extension of the monopole prescription is to include higher-order multipole moments. If the entire mass distribution is enclosed, then the potential can be expanded in a series of spherical harmonics  $Y_{lm}(\theta, \phi)$  (where  $\theta \in [0, \pi]$  is the usual polar angle with respect to the  $z$  axis and  $\phi \in [0, 2\pi)$  is the usual azimuthal angle with respect to the positive  $x$  axis):

$$\Phi(\mathbf{x}) = - \sum_{l=0}^{\infty} \sum_{m=-l}^l \frac{4\pi}{2l+1} q_{lm} \frac{Y_{lm}(\theta, \phi)}{r^{l+1}}, \quad (13)$$

where  $q_{lm}$  are the so-called multipole moments. The origin of the coordinate system is taken to be the center of the computational domain, and  $r$  is the distance to the origin. The multipole moments can be calculated by expanding the Green's function for the Poisson equation as a series of spherical harmonics. After some algebraic simplification of Equation 13, the potential outside of the mass distribution can be written as:

$$\Phi(\mathbf{x}) = - \sum_{l=0}^{\infty} \left\{ Q_l^{(0)} \frac{P_l(\cos \theta)}{r^{l+1}} + \sum_{m=1}^l \left[ Q_{lm}^{(C)} \cos(m\phi) + Q_{lm}^{(S)} \sin(m\phi) \right] \frac{P_l^m(\cos \theta)}{r^{l+1}} \right\}. \quad (14)$$

$P_l(x)$  are the Legendre polynomials and  $P_l^m(x)$  are the associated Legendre polynomials.  $Q_l^{(0)}$  and  $Q_{lm}^{(C,S)}$  are variants of the multipole moments that involve integrals of  $P_l$  and  $P_l^m$ , respectively, over the computational domain; their definition is given in Appendix C.

This approach becomes computationally feasible when we cut off the outer summation in Equation 14 at some finite value of  $l_{\max}$ . If it is of sufficiently high order, we will accurately capture the distribution of mass on the grid. In practice we first evaluate the discretized analog of the modified multipole moments for  $0 \leq l \leq l_{\max}$  and  $1 \leq m \leq l$ , an operation that scales as  $N^3$ . We then directly compute the value of the potential on all of the  $6N^2$  boundary zones. Since the multipole moments only need to be calculated once per Poisson solve, the full operation scales only as  $N^3$ . The amount of time required to calculate the boundary conditions is directly related to the chosen value of  $l_{\max}$ , so there is a trade-off between computational expense and accuracy of the result.

As a demonstration of the method's accuracy, we consider the case of two white dwarfs of mass ratio 2/3, using the initialization procedure described below in Section 3. We terminated the simulation just after initialization, so that we perform only an initial Poisson solve for this density distribution. We did this for values of  $l_{\max}$  ranging

from 0 to 20, and we also did this using the numerically exact solution provided by Equation 12. Defining the  $L^2$  norm of a field  $f$  as

$$\|f\|_2 = \left( \sum_{i,j,k} \Delta x \Delta y \Delta z f_{ijk}^2 \right)^{1/2}, \quad (15)$$

we computed the  $L^2$  error of  $\Phi$  on the entire domain for multipole boundary conditions, which we call  $\Phi_l$ , relative to  $\Phi$  obtained using the exact boundary conditions:

$$\text{Error}_l = \frac{\|\Phi_l - \Phi_{\text{exact}}\|_2}{\|\Phi_{\text{exact}}\|_2}. \quad (16)$$

The result is shown in Figure 1. At  $l_{\max} = 6$ , the error is already well below  $10^{-4}$  and we adopt this as our default choice for all simulations with Poisson gravity. In Section 4.4 we show that there are no gains to be had by increasing the accuracy further. At very high orders ( $l \gtrsim 18$ ) the approximation breaks down, as seen in Figure 1. This is a result of the ambient material on the grid. At each boundary point we assume that all of the mass on the grid is contained within a sphere whose radius is the distance from that boundary point to the center of the domain. This does not hold for boundary points in the centers of domain faces, because of the material in the domain corners. This can be fixed by using multiple mass shells at different radii, but the error is negligible in practice for the values of  $l_{\max}$  that we use.

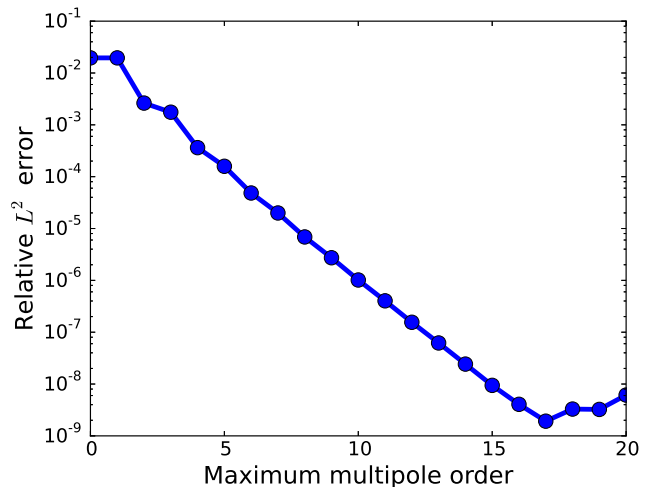


**Figure 1.** Error of  $\Phi$  on the computational domain for a binary white dwarf simulation whose boundary conditions were computed using various values of the maximum multipole order, relative to the exact solution determined by a brute force sum on the boundaries. Circles represent the error at integer values, and they have been connected by a smooth line to guide the eye.

### 2.3.3. Convergence Testing

Since the results of a merger simulation depend strongly on gravity, it is important to check whether proper numerical convergence is achieved for the Poisson solver. To do so, we created a simple test that initializes a sphere of radius  $R$  and uniform mass density  $\rho$  onto our grid, and used CASTRO to calculate the gravitational potential  $\Phi$  of this setup. We ensure that  $R$  is an integer multiple of the grid spacing, and the center of the sphere is at the origin. The problem domain for our simulations is  $[-1.6 \text{ cm}, 1.6 \text{ cm}]^3$ , and we take  $R = 1.0 \text{ cm}$  and  $\rho = 10^3 \text{ g cm}^{-3}$ . The zones with  $r > R$  are filled with an ambient material of very low density ( $10^{-8} \text{ g cm}^{-3}$ ). We run this problem at multiple resolutions corresponding to jumps by a factor of two. For comparison, at each grid point we evaluate the analytical potential of a uniform sphere, which can be easily determined using Gauss' law:

$$\Phi_{\text{sphere}}(r) = -\frac{GM}{r} \times \begin{cases} (3R^2 - r^2)/(2r^2) & r \leq R \\ 1 & r > R \end{cases}, \quad (17)$$

where  $M = 4\pi R^3/3$  is the mass of the sphere. We measure the numerical error by calculating the  $L^2$  norm of the error and normalizing it by the  $L^2$  norm of the analytical solution:

$$\text{Error} = \frac{\|\Phi - \Phi_{\text{sphere}}\|_2}{\|\Phi_{\text{sphere}}\|_2}. \quad (18)$$

We define the order of convergence  $p$  between two simulations with a jump in resolution of integer factor  $m > 1$  as

$$p = \log_m \left( \frac{\text{Error}_{\text{low}}}{\text{Error}_{\text{high}}} \right). \quad (19)$$

Here  $\text{Error}_{\text{low}}$  is the  $L^2$  error at the lower resolution and  $\text{Error}_{\text{high}}$  is the  $L^2$  error at the higher resolution. We expect the error to converge at  $p = 2$  given the discretization we choose. For all simulations in this section and for all our main science simulations, we choose a relative error tolerance of  $10^{-10}$  to be satisfied in the multigrid solve. The results of this test are plotted in Figure 2.

We find that at low resolution convergence is actually substantially better than second-order. The explanation for this is that we are attempting to model a spherical object on a rectangular grid. This results in two sources of error. First, at very low resolution, the object does not look very spherical due to the rectangular grid representation, so the potential it produces is not quite that of a sphere. As the resolution is increased, the distribution of the mass on the grid will change. Second, the total amount of mass on the grid will change as the sphere fills out. So we are combining the true accuracy bonus from increased resolution with the artificial accuracy bonus from getting closer to solving the problem we are supposed to be solving. At high resolution this effect levels

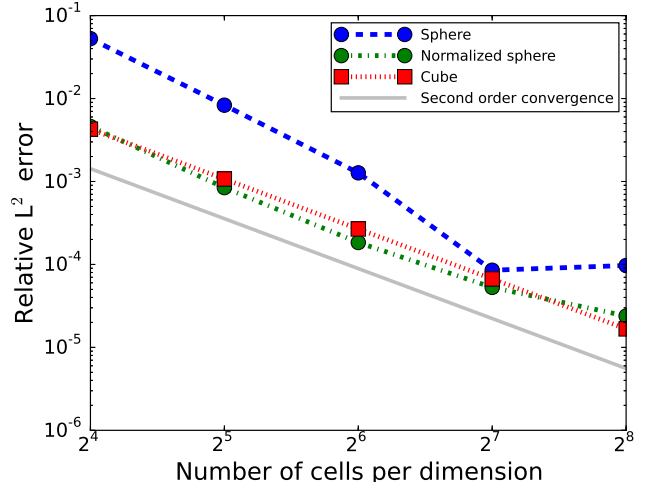


**Figure 2.** Comparison of the CASTRO gravitational potential to the analytical solution for: a sphere of uniform density; the same sphere, but with the potential normalized using the actual amount of mass on the grid instead of the mass of a perfect sphere; and, a cube of uniform density. Plotted also is a notional curve whose slope represents perfect second order convergence.

off, though, as the representation of the sphere is not significantly different in our two highest resolutions shown. For example, at 128 zones per dimension the amount of mass on the grid happens to be slightly closer to the true spherical mass than at 256 zones per dimension. We can eliminate the second source of error by changing the density on the grid so that the total mass  $M$  is actually what we intend it to be. The resolution study for this case (the “normalized sphere”) is also plotted in Figure 2. At low resolution we still obtain convergence slightly better than second-order, indicating that we have not eliminated the geometrical problem of the mass distribution changing.

The only way to fully eliminate this effect is to use a test problem that does not change with resolution. The obvious companion problem is a cube of uniform density  $\rho$ , where now  $R$  is half of the side length of the cube. At each resolution we use the same  $R$  as for the sphere, which ensures that the cube always fills exactly the same fraction of the domain and thus has the same mass, so the only improvement comes from better sampling at higher resolution. The gravitational potential for this object has been worked out analytically by Waldvogel (1976) (see also a similar result by Hummer (1996), and an earlier calculation by MacMillan (1958)). The potential is given

in Equation 15 of that paper<sup>5</sup>:

$$\begin{aligned} \Phi_{\text{cube}}(x, y, z) = & -G\rho \sum_{i,j,k=0}^1 \left[ x_i y_j \tanh^{-1} \left( \frac{z_k}{r_{ijk}} \right) \right. \\ & + y_j z_k \tanh^{-1} \left( \frac{x_i}{r_{ijk}} \right) + z_k x_i \tanh^{-1} \left( \frac{y_j}{r_{ijk}} \right) \\ & - \frac{x_i^2}{2} \tan^{-1} \left( \frac{y_j z_k}{x_i r_{ijk}} \right) - \frac{y_j^2}{2} \tan^{-1} \left( \frac{z_k x_i}{y_j r_{ijk}} \right) \\ & \left. - \frac{z_k^2}{2} \tan^{-1} \left( \frac{x_i y_j}{z_k r_{ijk}} \right) \right] \quad (20) \end{aligned}$$

where  $x_0 = R + x$ ,  $x_1 = R - x$ ,  $y_0 = R + y$ ,  $y_1 = R - y$ ,  $z_0 = R + z$ ,  $z_1 = R - z$ , and  $r_{ijk} = \sqrt{x_i^2 + y_j^2 + z_k^2}$ . We note that if implemented in Fortran or C/C++, the inverse hyperbolic tangent used here is `atanh` and the inverse tangent is `atan` (not `atan2`). This formula is valid both inside and outside the cube. The normalized  $L^2$  error for this problem is also shown in Figure 2, and only for this problem do we obtain perfect second-order scaling at all resolutions.

The main lesson here is that in a convergence study, it is important to ensure that the physical problem does not change with resolution. Since in the case of spherical objects on rectangular grids the effect may be to artificially boost convergence with resolution, in a simulation with spherical objects like stars one can envision a scenario of being fooled into believing apparently good convergence results that are simply a convolution of artificially high gravitational convergence and poor convergence in the hydrodynamics. A convergence study in this case is only fully valid if there is reason to be confident that this effect is negligible compared to other factors.

#### 2.4. Rotation

For the evolution of binary systems, it is most natural to evolve the two stars in a frame that is co-rotating at the same period as the orbital period. Since the publication of the original code paper, CASTRO now has the ability to evolve systems in a rotating reference frame. Source terms corresponding to the Coriolis and centrifugal force terms are added to the momentum and energy equations. In this frame, the stars essentially remain stationary in their original positions due to the centrifugal force supporting against the gravitational attraction, and will remain this way as long as significant mass transfer does not occur. Swesty et al. (2000) demonstrated (in the context of neutron star mergers) that conservation of angular momentum is much easier to obtain in the rotating reference frame than in an inertial frame

in which stars advect large amounts of material around the domain. We wish to emphasize that although it is commonly stated in the literature that fixed-mesh codes poorly conserve angular momentum, it is only generally true that mesh-based codes do not exactly conserve angular momentum when the equations are written in conservative form for linear momentum. Indeed, Motl et al. (2002) and Byerly et al. (2014) have evolved binary systems using the hydrodynamics equations written in a form that explicitly conserves angular momentum, and it is straightforward to convert an existing grid-based code to solve the system of equations that Byerly et al. present. Additionally, the extent to which angular momentum conservation is violated in our code is a function of the resolution. When the resolution is sufficiently high, excellent conservation properties can result. At reasonable resolution for a binary orbit our code conserves angular momentum well enough to keep the stars stable for a large number of orbits; however, at moderate resolution in an inertial frame, there is a secular loss of angular momentum that eventually will result in a spurious merger. We note that as the stars begin to coalesce, the rotating reference frame will no longer provide a good approximation to the spatial motion of the stars and then they will begin to significantly move around the domain. This is not necessarily problematic because the most important feature of the rotating frame is that it helps ensure that the initial coalescence is not the result of spurious numerical loss of angular momentum. When significant mass transfer sets in and evolution proceeds on a dynamical timescale, the conservation properties may be slightly worse but angular momentum conservation is also less important.

In a rotating reference frame with angular frequency vector  $\boldsymbol{\omega}$ , the non-inertial contribution to the momentum equation is:

$$\left. \frac{\partial(\rho\mathbf{u})}{\partial t} \right|_{\text{rot}} = -2\boldsymbol{\omega} \times (\rho\mathbf{u}) - \rho\boldsymbol{\omega} \times (\boldsymbol{\omega} \times \mathbf{r}). \quad (21)$$

Here  $\mathbf{r}$  is the position vector with respect to the origin. Typically we choose  $\boldsymbol{\omega} = (0, 0, 2\pi/T)^T$ , with the rotation axis coincident with the  $z$  axis at  $x = y = 0$ .  $T$  is the rotation period, which is the most natural quantity to specify for a rotating stellar system. As described in Appendix A, we include this source term in the edge state prediction in a way that is analogous to the gravity source. We evaluate all quantities at cell centers. We use the same predictor-corrector approach that we use for the gravity source terms to the momentum equations. A slight difference is that the Coriolis force for each velocity component is coupled to other velocity components. If the rotation is about the  $z$ -axis, then the discrete update to  $u^{n+1}$  depends on the value of  $v^{n+1}$ , and vice versa. If we fix the value of the time-level  $n + 1$  quantities after

<sup>5</sup> The last term in that equation is missing a factor of 1/2, which destroys the symmetry. We have inserted this missing factor and performed a simple coordinate transformation so that the center of the cube is at the origin.

coming out of the hydrodynamics update, there would be a slight inconsistency between the  $x$  and  $y$  components of the velocity.

We propose a more accurate coupling that directly solves this implicit system of coupled equations. We denote by  $(\widetilde{\rho\mathbf{u}})$  the value of the momentum after updating it with the centrifugal force, and the time-level  $n$  Coriolis force. The remaining update for the time-level  $n + 1$  Coriolis force then appears as:

$$(\rho\mathbf{u})^{n+1} = (\widetilde{\rho\mathbf{u}}) + \frac{\Delta t}{2} (-2\boldsymbol{\omega} \times (\rho\mathbf{u})^{n+1}) \quad (22)$$

To proceed further, we assume that the rotation is about the  $z$  axis with frequency  $\omega$ . Then there is no update to the  $z$ -momentum, and the other equations are:

$$(\rho u)^{n+1} = (\widetilde{\rho u}) + \omega \Delta t (\rho v)^{n+1} \quad (23)$$

$$(\rho v)^{n+1} = (\widetilde{\rho v}) - \omega \Delta t (\rho u)^{n+1} \quad (24)$$

We can directly solve this coupled system:

$$(\rho u)^{n+1} = \frac{(\widetilde{\rho u}) + \omega \Delta t (\widetilde{\rho v})}{1 + \omega^2 \Delta t^2} \quad (25)$$

$$(\rho v)^{n+1} = \frac{(\widetilde{\rho v}) - \omega \Delta t (\widetilde{\rho u})}{1 + \omega^2 \Delta t^2} \quad (26)$$

We use this form of the momentum update in **CASTRO**. This improvement is small but increases the accuracy of our rotating white dwarf systems over long time-scales.

The update to the energy equation can be determined by taking the dot product of the velocity with the momentum source terms. The Coriolis term vanishes identically, and so the Coriolis term does no work on the fluid. The update from the centrifugal force becomes

$$\left. \frac{\partial(\rho E)}{\partial t} \right|_{\text{rot}} = \frac{1}{\Delta V} \int \rho \mathbf{u} \cdot \mathbf{f}^R dV, \quad (27)$$

with  $\mathbf{f}^R \equiv -\boldsymbol{\omega} \times (\boldsymbol{\omega} \times \mathbf{r})$ . This expression is identical in form to the gravity source under the interchange of  $\mathbf{g}$  with  $\mathbf{f}^R$ . As observed by [Marcello & Tohline \(2012\)](#), we can similarly write down a rotational potential,

$$\Phi^R = \frac{1}{2} |\boldsymbol{\omega} \times \mathbf{r}|^2. \quad (28)$$

In the presence of rotation the conserved total energy becomes:

$$\int dV (\rho E_{\text{tot}}) = \int dV \left( \rho E + \frac{1}{2} \rho \Phi + \rho \Phi^R \right). \quad (29)$$

Given that we can write down a potential energy for the rotation field, then we can use the machinery of [Section 2.3.1](#). We again continue to evolve explicitly an equation for the gas energy, and allow it to change in response to work done by or on the rotational potential.

$$\Delta(\rho E)|_{\text{rot}} = -\frac{1}{2} \sum_f \Delta \rho_f (\Phi_{f+1/2}^R - \Phi_{f-1/2}^R) \quad (30)$$

We apply the rotational forces after the gravitational forces, but there is some freedom in the order in which to apply the gravitational and rotational terms. This order may matter because the Coriolis force depends on the fluid velocity, and in the predictor-corrector approach, we use the velocities both at time-level  $n$  and time-level  $n + 1$ . If we update the latter with the gravitational force, then the Coriolis force sees a different velocity than the one obtained through the pure hydrodynamics step. (The energy equation does not face the same issue in our new formulation, because the velocities used are always the time-level  $n + 1/2$  values coming from the Riemann solver.) In practice, this does not matter significantly for our simulations in this work because the centrifugal force plays the dominant role in maintaining stability of non-contact binary systems, and the centrifugal force does not depend on the fluid velocity. This issue may be worth exploring in future work in situations where the Coriolis term is non-negligible in determining the system evolution.

In all simulations performed in a rotating reference frame, we transform all relevant quantities back to the inertial reference frame when reporting them in analysis routines and visualization (though the data is saved to profiles while still in the rotating frame). In particular, for every zone we adjust the position, momentum, and energy to account for rotation. If the position is  $\mathbf{x}$  in the inertial frame and  $\mathbf{x}'$  in the rotating frame, and the rotation vector is  $\boldsymbol{\omega}$ , the transformation rules are:

$$\mathbf{x}(t) = \mathbf{R}\mathbf{x}'(t) \quad (31)$$

$$\mathbf{v}(t) = \mathbf{v}'(t) + \boldsymbol{\omega} \times (\mathbf{R}\mathbf{x}'(t)) \quad (32)$$

The rotation matrix  $\mathbf{R}$  is:

$$\mathbf{R} = \mathbf{R}_z(\theta_3)\mathbf{R}_y(\theta_2)\mathbf{R}_x(\theta_1) \quad (33)$$

where  $\mathbf{R}_x$ ,  $\mathbf{R}_y$ , and  $\mathbf{R}_z$  are the standard rotation matrices about the  $x$ ,  $y$ , and  $z$  axes, and  $\boldsymbol{\theta} = \boldsymbol{\omega}t$ .

### 3. PROBLEM DESCRIPTION AND SOFTWARE IMPLEMENTATION

In this section we describe our white dwarf merger software, and focus in particular on the initial white dwarf models ([Section 3.1](#)), the initial problem setup ([Section 3.2](#)), and analysis ([Section 3.3](#)) components.

The software used to generate the test problems in this paper (as well as the manuscript itself), **wdmerger**<sup>6</sup>, is freely available at an online repository hosting service. Version control in both the parent software (**BoxLib**, **CASTRO**) and in **wdmerger** permits us to reference the state of the code at the time a simulation was performed. In all plot files and diagnostic output generated

<sup>6</sup> **wdmerger** can be obtained at <https://github.com/BoxLib-Codes/wdmerger>.

by `CASTRO`, and figure files generated by `wdmerger`, we store the active `git` commit hashes of `BoxLib`, `CASTRO`, and `wdmerger`. Line plots are generated using the `matplotlib` library for `Python` (Hunter 2007), while slice plots and other multi-dimensional visualizations are generated using the `yt` code (Turk et al. 2011).

### 3.1. White Dwarf Models

At the start of any full simulation, we generate initial model white dwarfs by integrating the equation of hydrostatic equilibrium, taking the temperature to be constant, and using the stellar equation of state. This results in a single non-linear equation to find the density in a zone given the conditions in the zone beneath it:

$$\frac{p_{i+1} - p_i}{\Delta x} = \frac{1}{2}(\rho_i + \rho_{i+1})g_{i+1/2}. \quad (34)$$

This equation is a function of  $\rho_{i+1}$  only since the pressure is uniquely determined by the density in this case. Here,  $\rho_i$  and  $p_i$  are known, and  $g_{i+1/2}$  is the gravitational acceleration at the interface between zones  $i$  and  $i + 1$ , found by simply adding up all the mass from zones 1 to  $i$  to get the enclosed mass,  $M_{i+1/2}$ , and then setting  $g_{i+1/2} = -GM_{i+1/2}/r_{i+1/2}^2$ . We solve this equation for  $\rho_{i+1}$  using a Newton-Raphson iteration.

We desire to specify the mass of the white dwarf, as well as its temperature and composition. To start the integration off, we therefore need to guess at a central density. We then do a secant iteration over the entire integration procedure to find the central density needed to yield the desired total mass. The grid spacing is  $\Delta x = 6.25$  km. We chose this value because no simulation we perform is likely to exceed this grid resolution inside the stars themselves; for our normal domain size (see below), this corresponds to three jumps in refinement by a factor of four. We find that for low resolution runs, this is a better choice than selecting the 1D grid spacing to be comparable to the 3D grid spacing.

The white dwarf composition is determined by the chosen mass. For this paper we adopt the scheme of Dan et al. (2012). Low-mass WDs are pure helium; low-to-intermediate-mass WDs are an even carbon-oxygen core with a relatively large helium envelope; intermediate-mass WDs are a carbon-oxygen core with slightly more oxygen than carbon; and, high-mass WDs are composed of oxygen, neon, and magnesium. This choice of composition distribution broadly resembles the results of stellar evolution calculations in the respective mass ranges, though it does not match the calculations in detail.

We map the 1D model onto the 3D Cartesian grid by taking density, temperature, and composition as the independent variables, interpolating these to the cell centers, and then calling the equation of state to initialize

the remaining terms. It is possible to interpolate instead by using pressure instead of temperature, as pressure is more closely related to hydrostatic balance, but the EOS we use is so insensitive to temperature that this mapping can result in large deviations from the isothermal assumption we started with. The interpolation process divides each zone into  $n_{\text{sub}}$  sub-zones of equal volume for the purpose of sampling the 1D model, and the sub-zones are added together to obtain the full zone's state. This sub-grid-scale interpolation is useful especially near the edge of the star, where the density falls off rapidly with radius. Typically we take  $n_{\text{sub}} = 4$ .

### 3.2. Initial State

For a single star simulation, the star is simply placed at the center of the computational domain, which we take to be the origin. For a binary star simulation, we take as parameters the mass of the two white dwarfs and the initial orbital period  $T$ . Using Kepler's third law and assuming a circular orbit, we can then work out the orbital separation  $a$ :

$$a = \left( \frac{GMT^2}{4\pi^2} \right)^{1/3}. \quad (35)$$

Here  $M = M_P + M_S$  is the total mass of the system, where  $M_P$  is the specified *primary* mass and  $M_S$  is the specified *secondary* mass. The primary WD always starts on the left side of the computational domain for our simulations, and is more massive than the secondary. This reflects the usual terminology in the literature where the primary WD is the accretor and the secondary is the donor. The center of mass is located at the center of the computational domain, and by default the stars lie along the  $x$  axis, so that the primary's center of mass is located at  $x = -(M_S/M)a$  and the secondary's center of mass is located at  $x = (M_P/M)a$ . The user may choose to initialize the stars along a different axis, and can also choose a non-zero orbital phase and/or eccentricity.

The initial velocity is taken to be zero in if we are in the reference frame that rotates with the WDs, and if we are in the inertial frame the velocity in every zone is set equal to the rigid rotation rate corresponding to the distance of that zone from the rotation axis, given the specified period  $T$ . Thus the inertial frame and rotating frame simulations are starting off with the same initial conditions: two white dwarfs locked in synchronous rotation. This is the simplest assumption to make, but in the future we may explore relaxing this requirement.

In the current paper we do not attempt to enforce equilibrium with an additional relaxation step. This will be an important part of future work in this series, as numerous groups working on binary evolution (Swesty et al. 2000; Motl et al. 2002; Rosswog et al. 2004; Dan et al. 2011; Pakmor et al. 2012a) have commented on the im-

portance of equilibrium initial conditions in determining the evolution of the system. As a consequence of starting in a non-equilibrium setting, there are large density and pressure gradients near the white dwarf surfaces that result in significant amounts of mass flowing out of the white dwarfs. This can result in spurious non-physical consequences such as the total density or energy going negative in a zone. To compensate for this, we start the simulation with a timestep that is a few orders of magnitude smaller than that required by the CFL criterion, and allow the timestep to increase by 1% each timestep so that the timestep reaches its maximum allowed by the velocities on the grid over a span of approximately 1000 timesteps. This allows the gas at the surface of the white dwarf to come closer to equilibrium without having discontinuous jumps in the density or energy. For all simulations, the maximum timestep is set to be equal to one-half of the CFL limit.

The computational domain has a total size of  $1.024 \times 10^{10}$  cm in each spatial dimension, and is centered at the origin. Our coarse grid has  $256^3$  zones, corresponding to a spatial resolution of 400 km. For the present study, we choose a simple refinement strategy: on the coarse grid, all zones within twice the Roche radius of each star are tagged for refinement, using the formula provided by Eggleton (1983) for the effective Roche radius  $r_L$  of a star in a binary,

$$\frac{r_L}{a} = \frac{0.49q^{2/3}}{0.6^{2/3} + \ln(1 + q^{1/3})}. \quad (36)$$

In this formula we can use  $q = M_S/M_P$  for obtaining the Roche radius of the secondary, and use the inverse value of  $q$  to obtain the Roche radius of the primary. The extra buffer from doubling the Roche radius ensures that the sharp density gradients near the edge of the star are within the zone of refinement. On higher levels, we tag all zones above a given density threshold (taken to be  $1 \text{ g cm}^{-3}$  in this paper) that corresponds to the stars themselves. We also ensure that the outer part of the domain is never tagged for refinement. In future work we will add criteria that tag for refinement the gas between the stars, which is expected to feature nuclear burning.

Outside of the stars we fill the rest of the domain with a very low density ambient gas because our hydrodynamics model requires the density to be non-zero everywhere. This ambient material can create difficulties for the simulation. In addition to the negative densities or energies at the stellar surfaces mentioned earlier, in the rotating reference frame we observe that standing instabilities can create very large velocities in the ambient fluid that drag down the global timestep by up to an order of magnitude. To deal with this we employ a ‘‘sponge’’ similar to that described by Almgren et al. (2008) for the outer regions of the computational domain. After the hydrodynam-

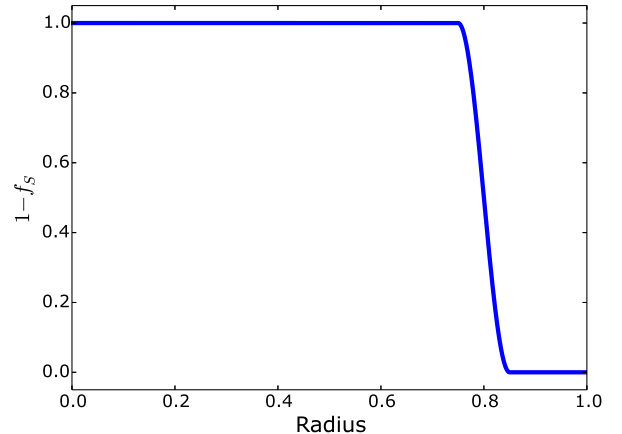


**Figure 3.** Radial profile of the hydrodynamical sponge we apply (Equation 38). We subtract  $f_S$  from unity; the value of  $1 - f_S$  indicates what happens to the sponged function after the sponge is applied. The sponge has no effect in the inner part of the domain, and is fully applied at the outer edge.

ics update, we apply a damping force to the momentum equation as follows:

$$(\rho \mathbf{u})^{n+1} \rightarrow \frac{(\rho \mathbf{u})^{n+1}}{1 + (\Delta t / \Delta t_S) f_S}, \quad (37)$$

where  $\Delta t_S$  is a timescale for the sponge to operate on, and  $f_S$  is the damping factor. We choose it so that the sponge is non-operational inside a radius  $r_S$  from the origin, and fully applied at a radius  $r'_S \equiv r_S + \Delta r_S$ . We then smooth the sponge out between  $r_S$  and  $r'_S$ :

$$f_S = \begin{cases} 0 & r < r_S \\ \frac{1}{2} \left( 1 - \cos \left[ \pi \left( \frac{r - r_S}{\Delta r_S} \right) \right] \right) & r_S \leq r < r'_S \\ 1 & r \geq r'_S. \end{cases} \quad (38)$$

For the simulations in this paper we set  $r_S$  to be 75% of the distance from the origin to the domain boundaries, and  $\Delta r_S$  so that the sponge smoothing region extends another 10% of that distance. The resulting profile is displayed in Figure 3. We set  $\Delta t_S = 0.01$  s, which is of the same order as the CFL timestep for typical problem setups. While the sponge is applied we should avoid imputing any physical meaning to what is happening in the low-density gas far from the stars.

### 3.3. Analysis

We track a number of diagnostic quantities at the end of coarse grid timesteps. For all simulations, we record the total energy (including the breakdown into its components: kinetic, internal, gravitational potential, and rotation); we note that for the diagnostics we actually use  $(\rho E)$  for calculation of the total energy, rather than

explicitly calculating the sum of kinetic and internal, as this is the quantity that should be explicitly conserved), the total angular momentum, and the center of mass of the system. We also separately record diagnostic information about the stars. Our strategy for tracking their locations is as follows: at the beginning of the calculation, we store the physical center of mass  $\mathbf{x}_c$  of the stars as determined by Kepler’s third law. We also store the velocity  $\mathbf{v}_c$  of the stars. Then, at each new time step we make a preliminary guess for their location by updating the location using the old velocity,  $\mathbf{x}_c \rightarrow \mathbf{x}_c + \mathbf{v}_c \Delta t$ . We then refine our guess for the location and velocity of each star by computing a location-weighted sum of the mass and velocity over the computational domain. To do this, we need a cutoff for determining what counts as part of the primary and what counts as part of the secondary. We use a simple criterion: the star that a zone “belongs” to is the one that exerts a larger magnitude gravitational force on that zone (as computed using the tentative data for that star’s mass and radius). From this we obtain the corrected mass of each star as well as its location and velocity. Once we have the new centers of mass, we compute the effective radius of each star at various density cutoffs. This involves computing the volume  $V$  of all zones that belong to the star (in the sense described above) whose density is greater than the cutoff. We then compute  $r_{\text{eff}} = (3V/4\pi)^{1/3}$ .

When we do simulations with adaptive-mesh refinement, there are multiple levels of refinement that contribute to a global integral. To deal with this we employ a “mask” which zeros out the data in a zone on a given level if there is a refined region overlying that zone.

### 3.3.1. Gravitational Waves

A final diagnostic quantity we consider is the gravitational wave emission by the binary system. White dwarfs are not strongly affected by general relativistic effects; the orbital motions are much slower than the speed of light, and the relativity parameter  $GM/c^2 R$ , which measures the ratio of the Schwarzschild radius of a mass  $M$  to the actual radius  $R$  of the object, is much less than unity for a white dwarf. Thus at any given time the relativistic effects are negligible compared to the Newtonian gravity and so we do not directly include relativistic effects in computing the dynamical evolution of the system. A white dwarf binary system does emit gravitational waves during its evolution; this energy loss is what drives the initial inspiral over very long timescales. Eventually it will drive the system to become dynamically unstable due to the Newtonian tidal forces alone, though once that period begins, the gravitational energy loss is inconsequential in affecting the dynamical evolution of the system. The frequency of the gravitational waves emitted by the white dwarf binary is similar to the frequency

of the orbital motion, which is in the range 10-100 mHz for our problem. This is well outside the range of currently existing gravitational wave detectors but is very well suited for proposed space-based detectors such as eLISA (Amaro-Seoane et al. 2013).

We follow the prescription of Blanchet et al. (1990) for computing a gravitational wave signal for our simulation. At distances far from the gravitational wave source, we can consider the leading term in the gravitational wave signal:

$$h_{ij}^{TT}(t, \mathbf{x}) = \frac{2G}{c^4 r} P_{ijkl}(\mathbf{n}) \ddot{Q}_{kl}(t - r/c). \quad (39)$$

$h$  is the perturbation to the spacetime metric and is commonly called the *strain*; for laser interferometers, it measures the relative change in the distance between mirrors. The “TT” superscript indicates that we work in the commonly used transverse-traceless gauge. This strain is measured at time  $t$  and position  $\mathbf{x}$  relative to the binary system.  $r \equiv |\mathbf{x}|$  is the distance from the observer to the binary system. The unit vector  $\mathbf{n} \equiv \mathbf{x}/r$  then measures the direction of the outgoing wave with respect to the observer, and  $P_{ijkl}(\mathbf{n})$  is an operator that projects a tensor onto the direction orthogonal to  $\mathbf{n}$ :

$$P_{ijkl}(\mathbf{n}) = (\delta_{ik} - n_i n_k) (\delta_{jl} - n_j n_l) - \frac{1}{2} (\delta_{ij} - n_i n_j) (\delta_{kl} - n_k n_l). \quad (40)$$

$Q_{kl}$  is the quadrupole moment tensor:

$$Q_{kl} = \int dV \rho \left( x_k x_l - \frac{1}{3} \delta_{kl} \mathbf{x}^2 \right). \quad (41)$$

The argument  $(t - r/c)$  indicates that to get the strain at time  $t$  we evaluate the second derivative of the quadrupole moment at the retarded time  $t - r/c$ . In practice the retarded time is simply the simulation time and the observer would see the gravitational waves after a time delay of order  $r/c$ .

Therefore the primary component of the calculation is the evaluation of the second time derivative of  $Q_{kl}$ . Explicitly constructing a discretized form of this derivative, using the current state and the state at previous times, is undesirable because of the inherent imprecision (its accuracy depends on the size of the timestep), in addition to the logistical challenges that may be implied by saving and using previous simulation states. Blanchet et al. (1990) provide a prescription for this time derivative purely in terms of the state at a given time:

$$\ddot{Q}_{kl} = \text{STF} \left\{ 2 \int dV \rho (v_k v_l + x_k g_l) \right\}. \quad (42)$$

The symmetric trace-free (STF) operator is defined as:

$$\text{STF} \{ A_{ij} \} = \frac{1}{2} A_{ij} + \frac{1}{2} A_{ji} - \frac{1}{3} \delta_{ij} \sum_k A_{kk}. \quad (43)$$



The strategy is then as follows. At the end of the coarse timestep, we first calculate  $\dot{Q}_{kl}$  using an integral over the domain. This quantity is independent of the observer. If we are using a rotating reference frame, we first convert velocities and positions back to the inertial frame before evaluating the integral. Then, we pick an observing location  $\mathbf{x}$  relative to the domain, evaluate the projection operator, and then perform the relevant tensor contraction to determine the strain tensor. We can repeat this process for any number of observing locations at minimal cost, since the quadrupole tensor only needs to be calculated once. Gravitational waves only excite modes orthogonal to their direction of travel. These are the “plus” and “cross” modes,  $h_+$  and  $h_\times$ , named after the types of spatial distortions they exhibit. We calculate the signal at a distance  $r$  along the  $x$ ,  $y$  and  $z$  axes. For the latter, as an example,  $h_+ = h_{11} = -h_{22} \propto (\ddot{Q}_{11} - \ddot{Q}_{22})/2$  and  $h_\times = h_{12} = h_{21} \propto \ddot{Q}_{12}$ . All other entries vanish. By default we take  $r = 10$  kpc; as shown by [Lorén-Aguilar et al. \(2005\)](#), this is a typical distance scale over which an experiment such as LISA could detect a coalescing binary white dwarf system. The strain at any other distance is easily calculated and goes as the inverse of the distance.

#### 4. NUMERICAL TEST PROBLEMS

White dwarf merger simulations face a number of numerical difficulties that are not present in single-degenerate Type Ia and core-collapse supernova simulations. In [Section 2.3](#), we discussed how the lack of spherical symmetry necessitates a careful look at the gravity solver. There are also hydrodynamical issues: the merger process will result in substantial motion of stellar material across the grid. This bulk motion presents an opportunity for advection errors to build up, and is only partially mitigated by evolving the white dwarfs in a co-rotating frame. It is therefore important to be aware of the behavior of the code in such circumstances. The behavior of **CASTRO** for many standard hydrodynamics test problems was detailed in the original code paper ([Almgren et al. 2010](#)), and in the interest of brevity we do not repeat them all here. Instead, we focus on a subset of problems that highlight the special difficulties introduced in merger simulations. These problems couple the hydrodynamics, gravity and equation of state modules. We observe that while in most non-trivial three-dimensional problems this creates a complexity that makes it impossible to determine exact analytical solutions, it is straightforward to devise problems for which certain global properties should obey simple, expected behaviors. Where possible, these should be quantified and a convergence study performed, and that is the focus of the current section.

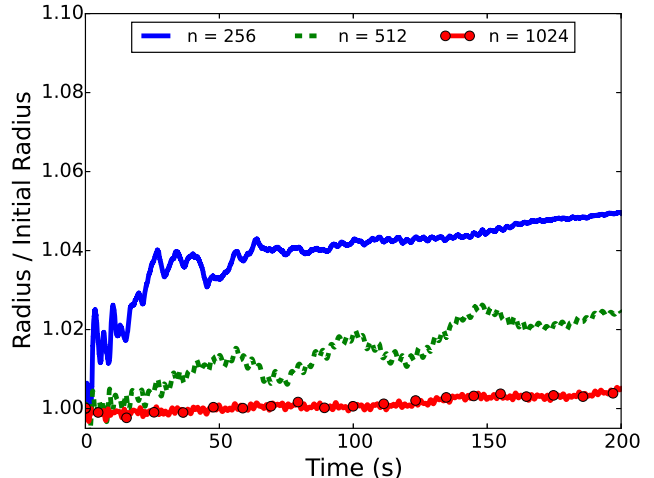


**Figure 4.** Time evolution of the effective radius of a  $0.9M_\odot$  white dwarf, seeded onto the grid using a one-dimensional hydrostatic model and evolved without further relaxation. The lines represent different number of zones per spatial dimension; when this number is greater than 256, it represents an effective resolution obtained using AMR levels that cover the star. The radius is determined using the volume of the grid that has a density greater than  $10^3 \text{ g cm}^{-3}$ .

##### 4.1. Maintaining Hydrostatic Equilibrium

In [Section 3.1](#) we describe the process by which we generate initial stellar models. While the 1D models are in hydrostatic equilibrium to within a small error, interpolation onto the 3D Cartesian grid will introduce perturbations into the solution ([Zingale et al. 2002](#)). Although we ensure that the initial models are generated with the same equation of state and are at least as well resolved as our finest grid, there is still be a hydrodynamical error associated with the fact that the rectangular grid cannot faithfully represent a spherical star. Additionally, the gravitational potential obtained by the multigrid solver will differ slightly from the one assumed by the initial model, and the operator splitting between the gravity and hydrodynamics should also result in small errors. As a result, we expect that the star will oscillate slightly about an equilibrium point, but that the amplitude of this oscillation should decrease with increasing resolution.

This problem was studied in the first **CASTRO** paper, but is worth revisiting here. A single star explosion simulation may only last a couple of seconds, and the **CASTRO** paper studied the behavior of the star after one second of evolution. However, the dynamical timescale of a typical carbon-oxygen white dwarf is on the order of 1–10 seconds. Additionally, a binary orbit is typically on the order of 10–100 seconds when a merger simulation

starts, and with equilibrium initial conditions the system may survive for tens of orbits before the secondary is disrupted. When this does happen, we want to be confident that it was because of the dynamics of the merger process and not because of an instability in an individual star. Our goal here is thus to install a single star onto our three-dimensional coordinate grid and evolve it for a period of time long enough to assess whether the star is truly stable, and to probe how the size of deviation from equilibrium is affected by grid resolution.

We loaded a single star of mass  $0.9 M_{\odot}$  onto the grid at the origin, and evolved it for 200 seconds. Our diagnostic of choice is the effective radius of the star, determined by the volume of the grid that has a density greater than  $10^3 \text{ g cm}^{-3}$  (see Section 3 for details on this measure). This choice of density is intended to mark a reasonable outer edge to the star that is not immediately susceptible to the numerical errors prevalent near the physical edge of the star. Figure 4 shows our results at various resolutions. As expected, the star quickly approaches an equilibrium size that is different (and in this case larger) than the one-dimensional model, though the magnitude of this change becomes smaller with resolution. The star is only approximately in equilibrium by this measure when the coarse grid of  $256^3$  zones has a level of refinement that jumps by a factor of four. Even then there is a slight uptick in the size toward the end, implying that the numerical stability is not guaranteed for arbitrarily long timescales. For another view, we consider the kinetic energy on the grid, in Figure 5. This is a more holistic measure that weights the contribution by the density. At the end of the simulation the kinetic energy is not lower at the highest resolution than at the lower resolutions. This result suggests that when constructing the equilibrium initial models that will form the basis of later calculations, we should carefully monitor the evolution of the stars when applying any artificial damping to cause the merger, to ensure that the merger is due to this applied force and not the intrinsic numerical instability of the stars.

#### 4.2. Gravitational Free Fall

A simple dynamical test to verify the coupling between the gravity and hydrodynamics in CASTRO is the case of gravitational free fall. We place two stars on the grid in the manner of Section 3. The distance  $a$  between them corresponds to a chosen orbital period  $T$ , consistent with the total system mass  $M$ , but we disable the rotational source terms so that the stars start at rest in an inertial reference frame. Thus the stars will simply begin moving toward each other. As long as the stars remain approximately spherical, the stars can be treated as point masses (this approximation only seriously breaks down after the stars have come into contact). In dimensionless

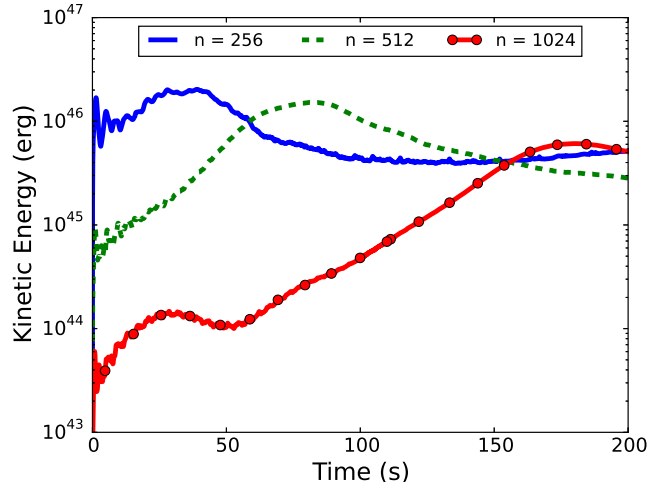


**Figure 5.** Time evolution of the kinetic energy of a  $0.9 M_{\odot}$  white dwarf. The lines have the same meaning as in Figure 4.

units where  $r \rightarrow r/a$  and  $t \rightarrow 2\sqrt{2}\pi t/T$ , the simple free fall equation of motion governing the distance  $r$  between their centers of mass takes the form:

$$\ddot{r}(t) = -\frac{1}{2r^2}. \quad (44)$$

It is possible to derive a closed-form solution for the evolution time as a function of separation by starting with the integral formulation,

$$t(r) = \int_1^r \frac{dr}{v(r)}. \quad (45)$$

The velocity  $v$  (in dimensionless units) can be found by noting that  $\ddot{r} = v dv/dr$  and then separating and integrating the equation of motion. This yields

$$v(r) = \sqrt{\left(\frac{1}{r} - 1\right)}. \quad (46)$$

For our problem  $0 < r \leq 1$ , so this is always valid. Integrating, we find

$$t(r) = \arccos(\sqrt{r}) + \sqrt{r(1-r)}. \quad (47)$$

so that the point of contact would occur at  $t = 1$ . We actually stop the simulation at  $t = 0.9$ , which is when the effects from the extended sizes of the stars starts to become important. The results of our simulation for our default  $256^3$  zone uniform grid are shown in Figure 6. They show excellent agreement between the analytical solution and the simulation results.

#### 4.3. Galilean Invariance

It is often stated in the literature that Eulerian methods for hydrodynamics with grids fixed in space do not obey the Galilean invariance of the underlying Euler

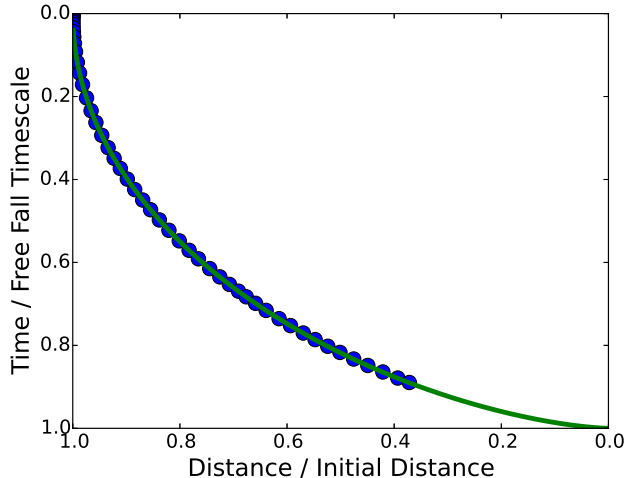


**Figure 6.** Time evolution of two initially stationary white dwarfs, mutually attracted to each other by the gravitational force. The horizontal axis gives the separation of the white dwarfs, scaled to the initial separation, and the vertical axis gives the elapsed time of the simulation, scaled to the time it would take two point masses to collide. The solid curve shows the analytical result, calculated from Newtonian mechanics, and the circles show the samples from the time evolution with `CASTRO`. For visual clarity, we show only a small fraction of the timesteps.

equations, so that simulations moving at a uniform bulk velocity appear different than an equivalent stationary simulation (e.g. [Springel \(2010\)](#)). If true, we need to understand the importance of this effect when deciding whether to trust the output of a code like `CASTRO` when applied for merger problems. Recently, concern for the issue of Galilean invariance has come up in two ways which are of note for us in the present study. We explain these situations and display the results of tests we have run to determine whether this actually is a significant concern for our study.

[Springel \(2010\)](#) (hereafter, S10) performed a Kelvin-Helmholtz instability test and showed that (at low resolution) a fixed-grid code failed to develop the expected fluid instability when the whole fluid was moving at a strongly supersonic uniform velocity. (See also [Wadsley et al. \(2008\)](#), who used the `FLASH` code to simulate a hot bubble subject to mixing by the Kelvin-Helmholtz instability, and also found that the mixing was affected by a uniform bulk velocity.) This contrasted with the results of the moving-mesh code `AREPO` being presented in that study, which demonstrated Galilean invariance even at large bulk velocities. Inability to correctly model the Kelvin-Helmholtz instability would have important consequences for how much we can trust the ability

of `CASTRO` to test the violent merger progenitor model, where a detonation arises in the low-density material at the stellar surface. Shearing between the material flowing out of the secondary and material near the surface of the primary may trigger fluid instabilities that play an important role in the evolution of that gas, which is the site of the initial detonation in the prompt explosion model. [Guillochon et al. \(2010\)](#) showed for their simulation that Kelvin-Helmholtz instabilities produced this way may raise the temperature of the accreting material enough to ignite a detonation. Therefore if we are not correctly reproducing the characteristics of the Kelvin-Helmholtz instability in the case where there is significant mass motion on the grid, we cannot be confident that a detonation (or lack thereof) is not numerically seeded.

[Robertson et al. \(2010\)](#) (hereafter, R10) observe that violation of Galilean invariance of simulation results for the Euler equations occurs because of truncation error in the discretization of the fluid equations. This takes the form of a numerical diffusion term which is dependent on velocity (and also resolution). The advantage of a moving-mesh code is that the mesh everywhere moves with the local flow velocity, which substantially reduces the numerical diffusion. R10 argue that the differences seen between the moving-mesh and fixed-grid code are caused by the interaction of this numerical diffusion with small-scale instabilities (that may be physical or numerical) which couple with and fundamentally alter the large-scale modes. Small-scale instabilities are seeded by the choice of a sharp initial discontinuity between the fluids in the problem posed by S10. Crucially though, R10 point out that this problem does not converge with resolution (because the initial perturbation is too sharp and seeds numerical noise at the grid resolution level) and so it is not possible to know the correct behavior of this problem. As such, we do not know whether the small-scale modes found in `AREPO` are real, and the problem is not useful in formally discriminating between methodologies. They instead propose an alternate test with a smoother initial contact. This converges to the same solution qualitatively in both the stationary and bulk velocity cases, indicating that the code does generally maintain Galilean invariance (to some specified error that depends on resolution and the uniform flow speed). We will see whether we can reproduce this result.

A related question is whether our code reliably simulates the bulk motion of the stars across the grid, and whether such bulk motion affects the stability of the star. This concern is prompted by the study of [Tasker et al. \(2008\)](#), who studied the effect of uniform translation on the stability of a spherically symmetric model for a galaxy cluster. They compared the radial profile of the cluster at initialization and after a period of time evolu-

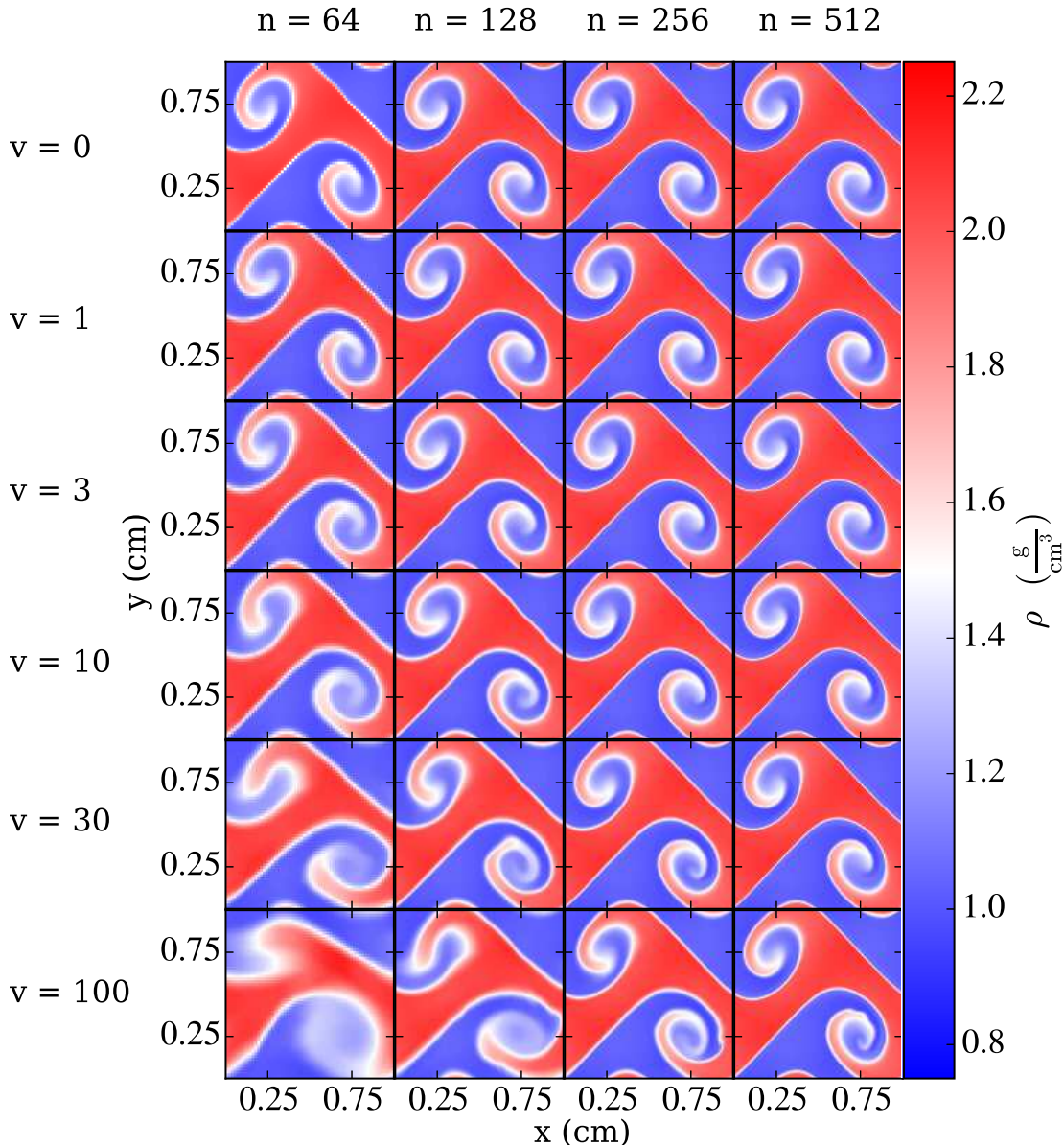


**Figure 7.** 2D Kelvin-Helmholtz instability test at  $t = 2.0$  for the initial conditions given by Equation 52 and Equation 54. The rows each represent a different bulk fluid velocity  $v$  and the columns each represent a grid resolution  $n$  (the number of zones per spatial dimension). The highest velocity simulation,  $v = 100$ , corresponds to approximately Mach 70. Compare to Robertson et al. (2010), Figure 7.

tion. Using FLASH and ENZO, they found that a static cluster retains its shape at high enough resolution, while uniform translation of the cluster causes mixing of the core material due to numerical diffusion which results in an underestimation of the core’s true density. The SPH codes they used did a better job maintaining the core density. We will perform a variant of this test using white dwarf models.

#### 4.3.1. Kelvin-Helmholtz Instability

Following Robertson et al. (2010), we set up a Kelvin-Helmholtz test in the following way. The problem domain runs from 0 to 1 in both the  $x$  and  $y$  directions.

This is a two-dimensional test, so we run CASTRO in 2D mainly to avoid extra computational expense; in 3D, it would merely involve replicating the problem in the  $z$  direction. The problem involves a fluid slab of density  $\rho_2 = 2.0$  traveling rightward in the  $x$ -direction at velocity  $v_2 = 0.5$ , sandwiched by a fluid of density  $\rho_1 = 1.0$  traveling leftward at velocity  $v_1 = -0.5$ . The density gradient is in the  $y$  direction, so this creates a velocity shear along the interface between the fluids. The density and velocity distribution on the computational domain are given by:

$$\rho = \rho_1 + R(y) [\rho_2 - \rho_1] \quad (48)$$

$$v_x = v_1 + R(y) [v_2 - v_1] \quad (49)$$

$$v_y = v_{\text{bulk}} + v' \quad (50)$$

Here  $R(y)$  is a ramp function that describes the transition between the two fluids, while  $v_{\text{bulk}}$  is the bulk motion of the fluid in the  $y$  direction and  $v'$  is the velocity perturbation that seeds the instability. The problem is established for two sets of initial conditions (ICs), which we follow R10 in calling ICs A and B. They differ in their ramp function ( $R_A$  and  $R_B$  respectively), as well as the initial perturbation ( $v'_A$  and  $v'_B$  respectively), and the frequency of the perturbation ( $n_A = 4$  and  $n_B = 2$ ):

$$R_A = \begin{cases} 0 & |y - 0.5| > 0.25 \\ 1 & |y - 0.5| < 0.25 \end{cases} \quad (51)$$

$$R_B = \left\{ \left[ 1 + e^{-2(y-0.25)/\Delta y} \right] \left[ 1 + e^{2(y-0.75)/\Delta y} \right] \right\}^{-1} \quad (52)$$

$$v'_A = w_0 \sin(n_A \pi x) \left\{ e^{-(y-0.25)^2/2\sigma^2} + e^{-(y-0.75)^2/2\sigma^2} \right\} \quad (53)$$

$$v'_B = w_0 \sin(n_B \pi x). \quad (54)$$

Here  $w_0 = 0.1$  is the scale of the velocity perturbation,  $\sigma = 0.05/\sqrt{2}$  controls the width of the Gaussian for IC A, and  $\Delta y = 0.05$  is the transition distance scale for the smooth ramp of IC B. The pressure everywhere is set to  $p = 2.5$ , and we run this with a gamma-law equation of state set to  $\gamma = 5/3$ . Plotfiles are generated every 0.05 seconds, and the problem is run until  $t = 2$ .

We run the problem for  $v_{\text{bulk}} = [0, 1, 3, 10, 30, 100]$ , and for each set of initial conditions run the problem at resolutions of  $64^2$ ,  $128^2$ ,  $256^2$ ,  $512^2$ . For context, in these units the sound speed is  $c \approx 0.7$ . In addition, for each initial condition we run simulations at the higher resolutions of  $1024^2$ ,  $2048^2$ , and  $4096^2$  for the stationary problem only. These serve as a reference solution to gauge the extent to which the bulk flow affects the development of the fluid instability, and to determine if the problem is numerically converged.

We find the same result as R10 for IC A, which is equivalent to the test proposed by S10: at low resolutions and high bulk velocity, the Kelvin-Helmholtz instability completely fails to develop. Furthermore the problem does not converge even qualitatively at the highest resolutions we used. Our results are very similar to Figure 3 of R10 so we do not show them here. For IC B, our results can be seen for the normal resolutions and all velocities in Figure 7. At low resolutions and very large bulk velocities, the fluid does get significantly disrupted by numerical error. This effect quickly converges away

with resolution and qualitatively at  $512^2$  resolution the solution is nearly identical to the stationary  $v = 0$  problem. We agree with R10 that this problem does converge with resolution and is not subject to numerically-seeded secondary instabilities at the stopping time. This is evident even at low resolutions by examining the first row of Figure 7.

McNally et al. (2012) published another Kelvin-Helmholtz problem that is well-posed in the sense that it converges with resolution and is not subject to uncontrollable numerical instabilities. Though they were not explicitly interested in the question of Galilean invariance, we visit that issue here to see what can be learned. The initial conditions for this problem are:

$$\rho = \begin{cases} \rho_1 - \rho_m e^{(y-0.25)/\Delta y} & 0.25 > y \geq 0 \\ \rho_2 + \rho_m e^{(0.25-y)/\Delta y} & 0.5 > y \geq 0.25 \\ \rho_2 + \rho_m e^{(y-0.75)/\Delta y} & 0.75 > y \geq 0.5 \\ \rho_1 - \rho_m e^{(0.75-y)/\Delta y} & 1 > y \geq 0.75 \end{cases} \quad (55)$$

$$v_x = \begin{cases} v_1 - v_m e^{(y-0.25)/\Delta y} & 0.25 > y \geq 0 \\ v_2 + v_m e^{(0.25-y)/\Delta y} & 0.5 > y \geq 0.25 \\ v_2 + v_m e^{(y-0.75)/\Delta y} & 0.75 > y \geq 0.5 \\ v_1 - v_m e^{(0.75-y)/\Delta y} & 1 > y \geq 0.75 \end{cases} \quad (56)$$

$$v_y = w_0 \sin(4\pi x). \quad (57)$$

Here  $\Delta y = 0.025$ ,  $w_0 = 0.01$ ,  $v_m = (v_1 - v_2)/2$ ,  $\rho_m = (\rho_1 - \rho_2)/2$ , and the other symbols have the same meaning as above (this means the flow direction is reversed compared to the original paper, so as to achieve consistency with the other simulations presented here). We run this problem at all the same resolutions and bulk velocities as the previous two problems. The results for the normal resolutions at  $t = 2.0$  are displayed in Figure 8. We see a similar pattern as for the test proposed by R10: as we get to higher flow speeds we need to have higher spatial resolution to compensate for the increased numerical diffusion. The qualitative accuracy is much lower for the highest bulk velocities for this problem than for the previous problems. This is because the amplitude of the instability overall is smaller than for the previous problems, at least by  $t = 2.0$ , so it is easier for numerical diffusion at the shearing layer, caused by the high bulk velocities, to completely wipe out the instability. Like Robertson et al. (2010) found for their problem, we find for this problem that the convergence properties are not substantially affected by altering the perturbation frequency – the results show the same qualitative pattern even if we halve this frequency.

Hopkins (2015) performed this test as part of the testing of their code GIZMO. They showed the late-time evolution of this system, when non-linear effects have taken

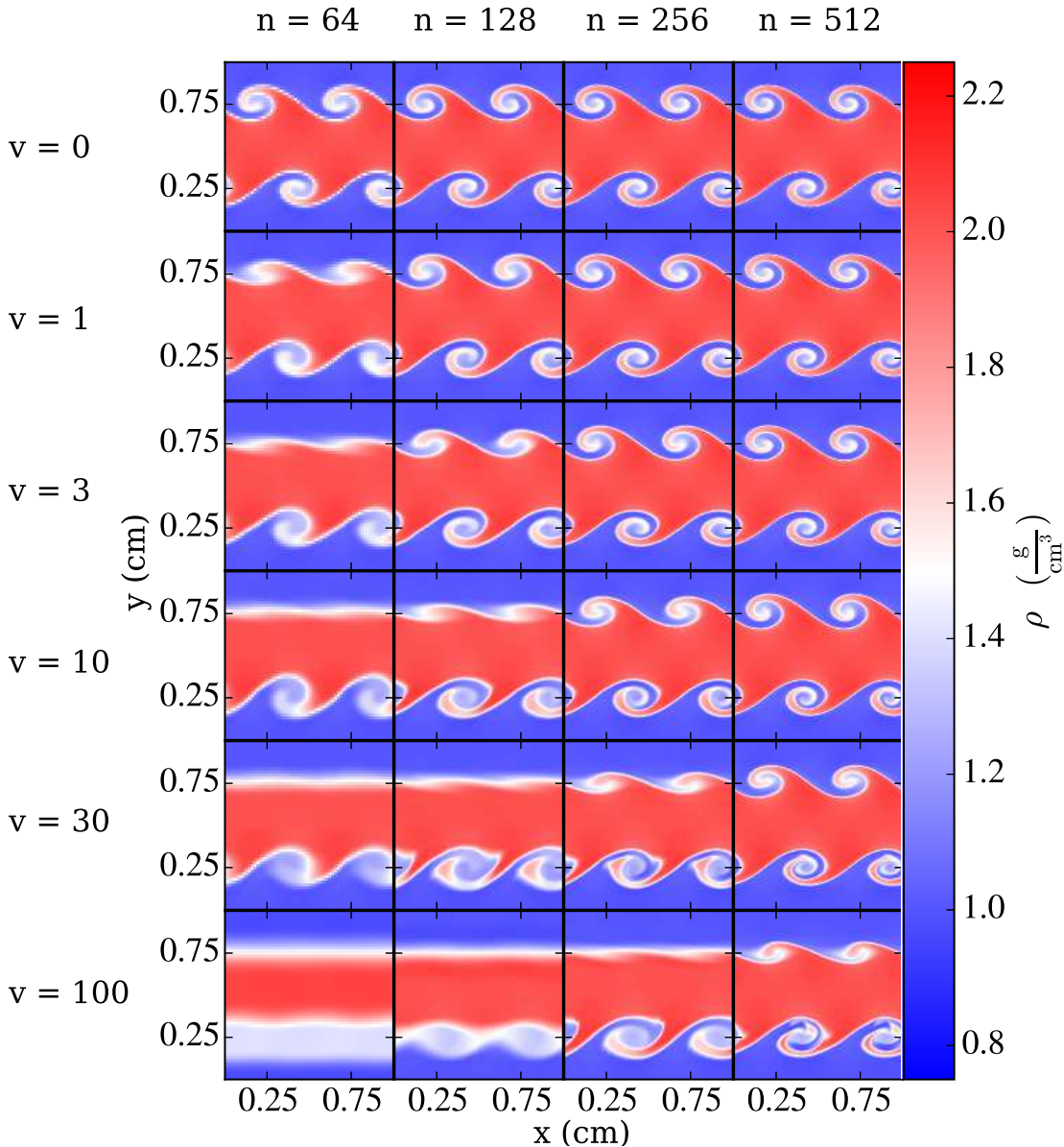


**Figure 8.** 2D Kelvin-Helmholtz instability test at  $t = 2.0$  for the initial conditions given by Equation 55 through Equation 57, which come from McNally et al. (2012). The meaning of the rows and columns is the same as in Figure 7.

over and significantly disrupted the initial flow. At low resolution the tested grid algorithm had failed to disrupt both for  $v = 0$  and  $v = 10$ . We too ran this problem until  $t = 10$ , and confirm that the Kelvin-Helmholtz instability damps out at low resolution but goes strongly non-linear and disrupts the flow at high resolution. We strongly emphasize the point that this does not objectively demonstrate a deficiency in fixed-grid codes for this problem. We can only determine the validity of a method when we have a trustworthy, converged solution to compare to, and this is lacking for this problem at late times. As observed by McNally et al., this lack of a solution is because the secondary instabilities form for this problem

when the whorls of the Kelvin-Helmholtz tendrils stretch out and create gradients that approach the grid resolution. This is prime breeding ground for numerical noise. But because the nature of this noise depends on the resolution, it is very different for simulations at different resolutions. If these instabilities are seeded because of this resolution-dependent noise and are not seeded instead in a controlled manner such that they appear at the same time and location, then we simply cannot draw any conclusions that bear on the question of verification from this test at late times. Figure 9 provides a sense of this by examining the crucial time at which the transition from the linear to the non-linear regime is occurring. At

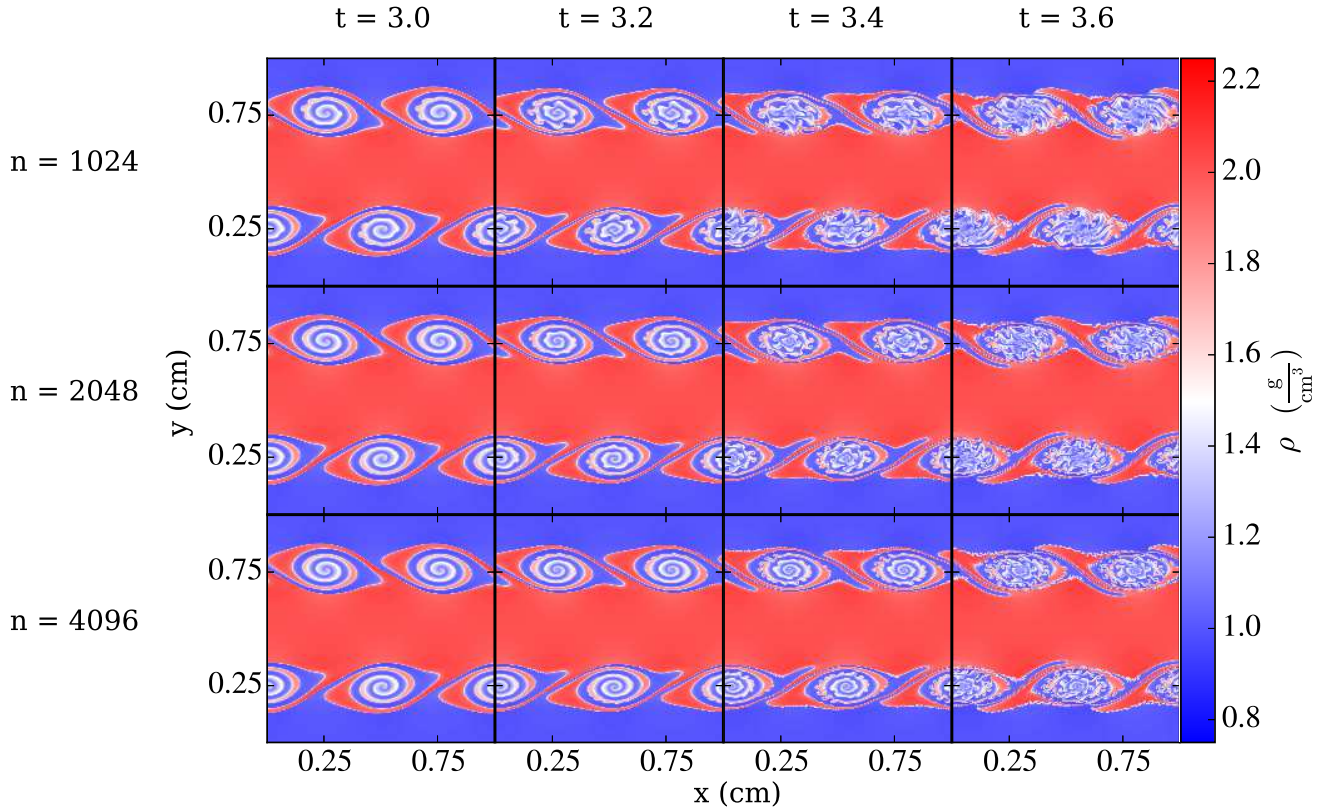


**Figure 9.** Time series of the Kelvin-Helmholtz problem proposed by McNally et al. (2012) as the simulation is just starting to go non-linear. The rows represent resolution, where  $n$  is the number of grid cells per spatial dimension, and the columns are different snapshots in time.

all of these very high resolutions the secondary instabilities develop, but they occur at different times and have different spatial scales for each resolution.

We conclude that large bulk motions of fluid can have very significant effects on numerical calculations of shear mixing in fixed-grid codes, but that this effect diminishes with increasing resolution. As a result, we must be confident that we are sufficiently resolving the major mixing regions on the white dwarf surfaces, specifically that the density gradients occur over spatial scales much larger than the grid resolution. If we find instead that this mixing occurs near the grid resolution scale, this will imply that we need to ramp up the resolution in these regions using AMR. If this becomes too expensive, we would need to be skeptical of any conclusions that could be drawn about the effect of the mixing on the nuclear burning.

#### 4.3.2. Moving Star

To analyze the effects of velocity-dependent results for a stellar simulation, we repeated the test of Section 4.1 with a bulk velocity on the grid. We chose a velocity of  $2.56 \times 10^8 \text{ cm s}^{-1}$ . For context, this is comparable to the orbital velocities of the stars in Section 4.4, and the Mach

number is of order unity in the stellar core at this speed. This test was inspired by Tasker et al. (2008), who considered a moving galaxy cluster and who obtained a long timescale evolution by using periodic boundary conditions, so that the cluster would cross the domain multiple times throughout the evolution. We believe that periodic boundary conditions are unrealistic for our type of simulation, so we prefer to do one continuous simulation where the star does not cross the boundaries. Since our normal grid was not large enough to allow the motion to continue for very long, we expanded the domain size by a factor of four, and then included an extra refined level around the star to keep the effective resolution the same. We started the star off in the lower left corner of the domain, and pointed its velocity towards the upper right corner. This allowed us to evolve the star for the same length of time as for the original test. We note that getting the gravity boundary conditions right required us to move the origin of the problem at the bulk velocity, so that the multipole moments were always computed with respect to the current location of the stellar center.

In Figure 10, we take the results of Section 4.1 (the “static” case), and plot on top of it the results of this new simulation (the “motion” case). We see immediately

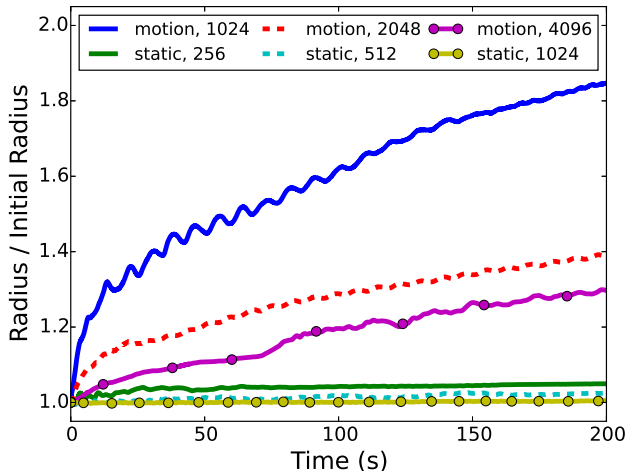


**Figure 10.** A variation on [Figure 4](#) where we now compare the “static” case to “motion” simulations where the star moves across the grid at a fixed linear speed. The lines represent the effective number of zones per dimension inside the stellar material; due to the expanded size of the grid in the “motion” case, the physical resolution is the same in each column in the legend.

that this bulk velocity causes the star to be much worse at maintaining hydrostatic equilibrium. Not only is the absolute size of the star significantly larger (nearly a factor of two at the lowest feasible resolution we consider), but also there is a clear upward trend in the size that has not terminated at any resolution by the end of the simulation. This again emphasizes the results mentioned earlier, that we must be careful not to trust any simulation with significant mass transfer if we are not confident that the mass transfer is seeded in a controllable manner and free from numerical noise.

#### 4.4. Keplerian Orbit

We now consider the phase of the binary system where the stars are orbiting each other at distances great enough that the initial orbits should be approximately Keplerian. There are a number of effects worth looking into here. For simplicity, we choose two cases to demonstrate the simulation behavior: an equal mass case of two  $0.9 M_{\odot}$  white dwarfs, and an unequal mass case of  $0.9 M_{\odot}$  and  $0.75 M_{\odot}$  white dwarfs. In both systems, the secondary should be stable against mass loss. In each case, the initial orbital period is 100 seconds.

For some of the algorithms described earlier in this work, a single orbit of these systems is enough to examine their effects. In [Section 2.3.2](#), we discussed the replacement of a monopole boundary condition solver for the gravitational potential with a more general multipole solver for the boundaries. To test the relevance of this effect, we considered a single orbit of the unequal mass

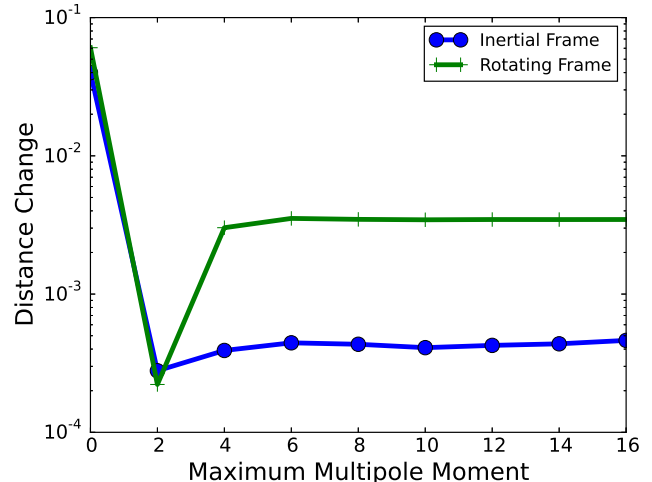


**Figure 11.** Absolute magnitude of the relative change in the distance of two unequal mass white dwarfs after one orbital period. The stars were evolved in an inertial reference frame. The horizontal axis is the number of terms or multipole moments captured in the series expansion for the potential at the domain boundary.

system and measured the distance between the two white dwarf centers of mass at the beginning of the simulation and after the full orbital period. This distance should not change significantly over that timescale. We performed this test for maximum multipole moments ranging from 0 (the monopole term) to 16. The results are shown in [Figure 11](#). Terms in the boundary potential that vary faster than  $r^{-5}$  are effectively negligible in determining the outcome of the orbit, justifying our typical choice of maintaining terms up to  $r^{-7}$ .

Another diagnostic that we consider is the energy conservation of the system. Recalling [Section 2.3.1](#), there are several different methods of applying the gravitational source term to the hydrodynamics equations. In `CASTRO` we presently have four options, controlled by the parameter `castro.grav_source_type`, which we shorten to `gs` for the present discussion. `gs = 1` and `gs = 2` are variations on the standard cell-centered source term for gravity. The difference between them is that `gs = 2` determines the value of the energy source term after the momentum source term has been applied, while `gs = 1` uses the uncorrected momenta in calculating  $\rho \mathbf{u} \cdot \mathbf{g}$ . We have found `gs = 2` to be more accurate. `gs = 3` is entirely different: after calculating the new momenta, we reset the total energy to be equal to the internal energy plus the kinetic energy. This approach has the virtue of ensuring that there is no conflict due to discretization between the momentum and energy equations, and also correctly ensuring that the gravitational force does not directly change the internal energy—and thus the



temperature—of the fluid. However, it explicitly sacrifices total energy conservation. `gs = 4` is the new conservative method of evaluating the energy source terms at cell faces. The results for the change in energy after a single orbit are seen in the first column of [Table 4.4](#). The first two versions give reasonable and similar levels of energy conservation. The third has total energy changes on the order of 100%, but this itself does not have a severe effect on the dynamics because in this scheme the total energy variable is effectively a placeholder value of the kinetic energy plus internal energy, rather than being evolved directly. The last scheme is nearly two orders of magnitude better in energy conservation, justifying the effort in varying the scheme.

In [Table 4.4](#) we show also the effects on energy conservation of using the inertial reference frame. We use `rs` for the CASTRO parameter `castro.rot_source_type`. Each option for `rs` is implemented in the same way as for the gravitational source term, simply swapping out the gravitational acceleration for the rotational acceleration (except for the improvement to the momentum update for `rs = 4` described in [Section 2.4](#)). The `rs = 0` column means that rotation is turned off and we are in the inertial frame. We see that the choice of rotational coupling is much less important than the choice of gravity coupling. The “conservative” `rs = 4` is slightly better in energy conservation than the non-conservative, cell-centered `rs = 2` algorithm, but it is a small effect.

We are most interested in the stability of these systems over long timescales. To this end, we consider the same systems as above, but evolve them for 25 orbital periods. In [Figure 12](#) we illustrate the evolution of these systems by plotting the center of mass locations of the white dwarfs on the orbital ( $xy$ ) plane. For the equal mass case in the inertial reference frame, the curves fall nearly on top of each other for most of the run, indicating that the stars are indeed orbiting at the initial distance, at least for a while. Towards the end of the run, however, the orbit starts to decay significantly, and the center-of-mass distance of the two stars has decreased by about 10% after 25 orbits. We attribute this to non-conservation of angular momentum, which occurs because our code only explicitly conserves linear momentum. This orbital decay resembles the effect seen by [Swesty et al. \(2000\)](#) for the case of neutron stars. In the unequal mass case, the magnitude of the orbital decay is smaller but at the end of the run the secular decline in distance is also visible. In both cases the stars would likely merge due to numerical error after a long enough timescale.

The co-rotating frame is different. For clarity of visualization, we rotate these results back into the inertial frame before displaying their orbits. In both the equal and unequal mass cases, the centrifugal force pushes the stars outward toward a new equilibrium distance that is

a few percent larger than its initial distance. At the end of the run, the system is relatively stable, with oscillations about the new equilibrium distance. In fact these oscillations occur too in the inertial frame, but they are much more pronounced here. In the unequal mass case this is coupled with severe precession of the orbit, which results in chaotic-looking orbits when viewed from the rotating reference frame. These result from the explicit numerical consideration of the Coriolis and centrifugal terms, which do not appear in the inertial frame. So while the rotating frame is clearly more stable against mass transfer than the inertial frame, the cost is that the specific dynamics may be more suspect.

Turning to the conservation properties of the system, we examine as fairly typical cases the equal mass system in the inertial frame for energy conservation ([Figure 13](#)), and the unequal mass system in the rotating frame for angular momentum conservation ([Figure 14](#)). For the former system angular momentum is conserved to within 10 percent over the 25 orbits, while energy conservation is about an order of magnitude better. We note that while this is already a fairly good level of energy conservation, it is not nearly as good as the results of [Marcello & Tohline \(2012\)](#). This is because we reset the internal energy to a level corresponding to our temperature floor when it goes negative, while [Marcello & Tohline](#) do not reset and instead ignore the internal energy if it is negative. The resets impose an artificial floor on our ability to conserve energy, but they only happen in low-density regions and do not much affect the large-scale dynamics. Meanwhile, relative angular momentum conservation is not quite as good as relative energy conservation. This is linked to the decline (or increase) in the size of the orbit. This implies that we ought to be careful in concluding that at these moderate resolutions we can safely evolve systems for many dozens of orbits; this needs to be verified to ensure that an observed inspiral and merger is physically (not numerically) motivated.

As a simple verification test to ensure our gravitational wave calculations are correct, we plot the gravitational wave strain along the rotation axis for the first two periods of an unequal mass system. At this early time the orbit is circular and so to a good approximation we expect that the gravitational wave signal should be that of two point masses, whose positions are:

$$\mathbf{r}_P(t) = -a_P \cos(\omega t) \hat{x} - a_P \sin(\omega t) \hat{y} \quad (58)$$

$$\mathbf{r}_S(t) = a_S \cos(\omega t) \hat{x} + a_S \sin(\omega t) \hat{y}. \quad (59)$$

Then the mass distribution is  $\rho(\mathbf{r}) = M_P \delta^3(\mathbf{r} - \mathbf{r}_P) + M_S \delta^3(\mathbf{r} - \mathbf{r}_S)$ . From this it is straightforward to calculate the quadrupole tensor, take its second time derivative, and then apply the projection operator to get the gravi-

**Table 1.** Change in energy after a single orbit, i.e.  $|\Delta E/E|$ . “rs” is shorthand for the code parameter `castro.rot_source_type` and “gs” is shorthand for the code parameter `castro.grav_source_type`. The parameter meanings are explained in the main text.

	rs = 0	rs = 1	rs = 2	rs = 3	rs = 4
gs = 1	$4.8 \times 10^{-2}$	$4.6 \times 10^{-2}$	$4.6 \times 10^{-2}$	$4.6 \times 10^{-2}$	$5.7 \times 10^{-2}$
gs = 2	$4.9 \times 10^{-2}$	$4.6 \times 10^{-2}$	$4.6 \times 10^{-2}$	$4.6 \times 10^{-2}$	$5.7 \times 10^{-2}$
gs = 3	$1.1 \times 10^0$	$2.8 \times 10^0$	$2.8 \times 10^0$	$2.8 \times 10^0$	$2.8 \times 10^0$
gs = 4	$4.4 \times 10^{-4}$	$1.3 \times 10^{-3}$	$1.3 \times 10^{-3}$	$3.1 \times 10^{-4}$	$1.0 \times 10^{-3}$

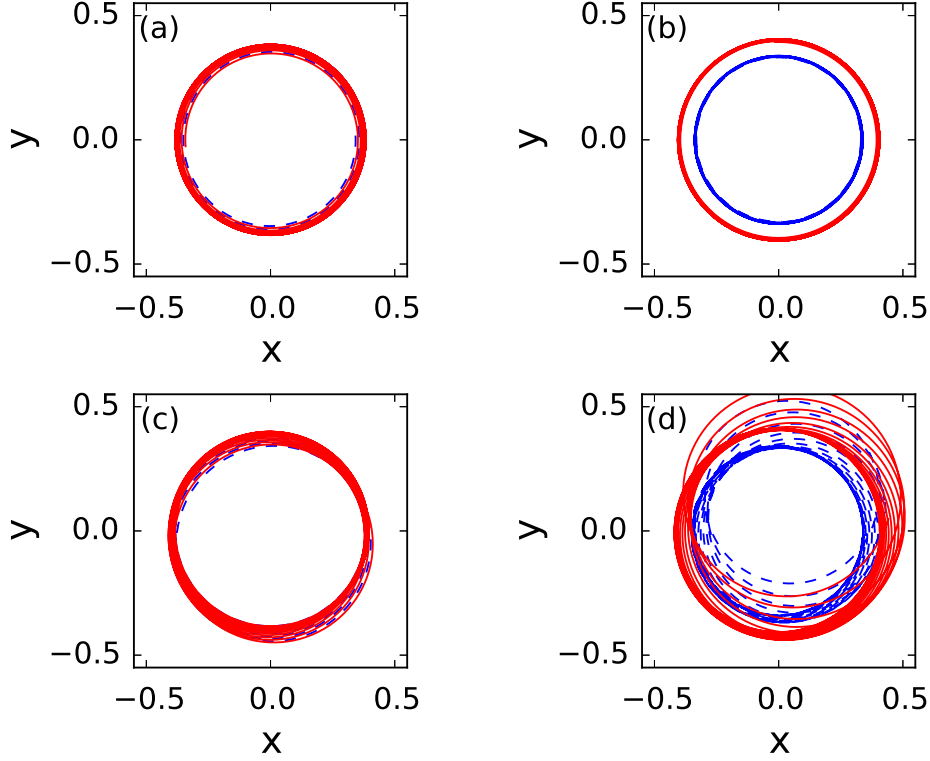


**Figure 12.** Positions of the white dwarfs in the orbital plane for four cases evolved over 25 orbital periods. The  $x$  and  $y$  axes are normalized to the size of the domain, so that  $x = -0.5$  is the left edge and  $x = 0.5$  is the right edge. The dashed blue curve is the position of the primary white dwarf, and the solid red curve is the position of the secondary. In plot (a) we have the equal mass system evolved in the inertial reference frame, and in plot (c) we have the same system evolved in a rotating frame, where the positions have been transformed back to the inertial frame for comparison. Plots (b) and (d) are analogous but for the unequal mass system.

tational wave polarizations along the rotation axis:

$$h_+ = -4 \frac{G\mu}{c^4 r} [GM_{\text{tot}}\omega]^{2/3} \cos(2\omega t) \quad (60)$$

$$h_\times = -4 \frac{G\mu}{c^4 r} [GM_{\text{tot}}\omega]^{2/3} \sin(2\omega t). \quad (61)$$

$\mu$  is the reduced mass, while  $M_{\text{tot}}$  is the total mass. From this we see that the gravitational wave frequency is twice the orbital frequency, and that the two polarizations are out of phase by  $90^\circ$  in time. We compare this analytical expectation to the numerical results in Figure 15. We

find very good agreement in this case, and this level of agreement holds in the rotating frame as well.

Finally we consider whether the dynamical behavior of the system converges with resolution. In Figure 16 we plot the first full orbit for the unequal mass system, at three different resolutions in the inertial frame: our default resolution of  $256^3$  zones, as well as a single level of refinement with a jump by a factor of two (effective resolution  $512^3$ ) or a jump by a factor of four (effective resolution  $1024^3$ ). It is clear that at the latter resolu-

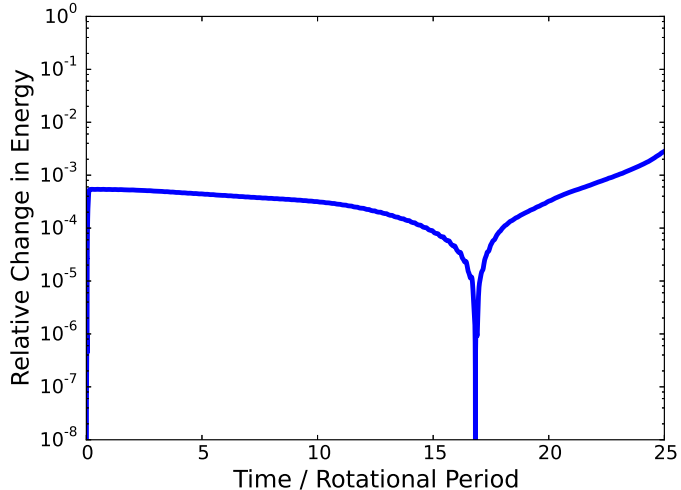


**Figure 13.** Absolute magnitude of the relative change in energy of two equal mass white dwarfs through 25 orbital periods, evolved in an inertial reference frame. The decline and recovery is a change in sign of the energy difference.

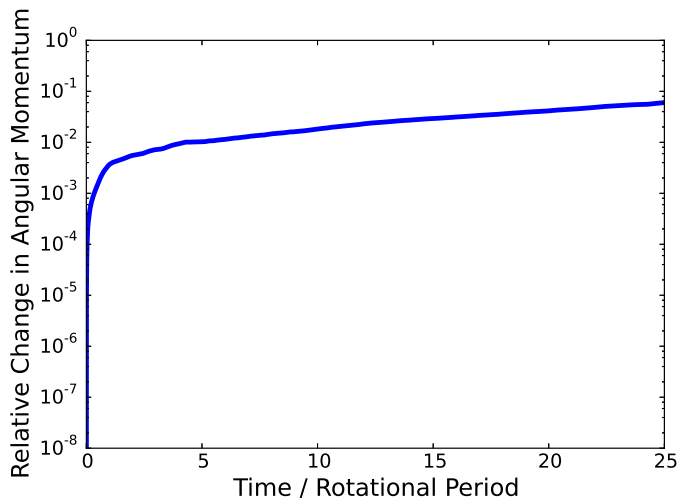


**Figure 14.** Absolute magnitude of the relative change in angular momentum of two unequal mass white dwarfs after 25 orbital periods, evolved in a co-rotating reference frame. We consider only the component of the angular momentum along the rotational axis.

tion (corresponding to physical resolution of 100 km), we have achieved convergent behavior. In the rotating frame, the results also show convergent behavior but the convergence is not as fast with resolution as in the inertial frame; see Figure 17. At the two higher resolutions the white dwarf distance is qualitatively similar, and both are qualitatively different from the lower resolution. However, quantitatively the two higher resolution runs are not as similar to each other as the analogous

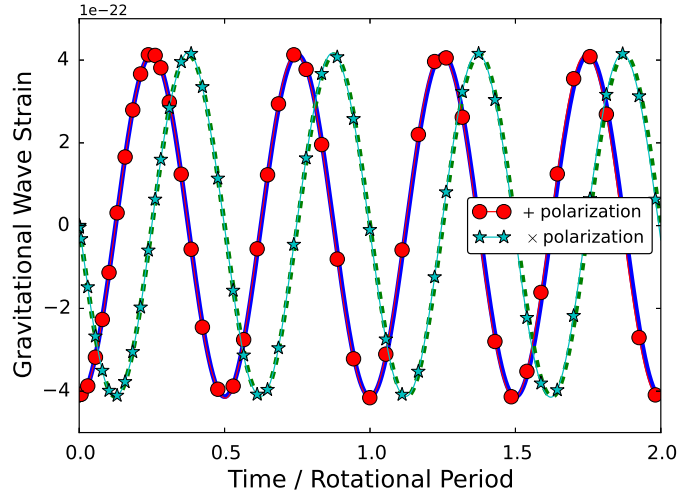


**Figure 15.** Gravitational wave strain polarizations for the first two orbital periods of an unequal mass system. The curves with markers are the numerical data, while the curves without markers are the analytical results for two point masses.

runs in the inertial frame. Convergence with resolution is slightly slower in the rotating reference frame because in the rotating reference frame a stable, unchanging circular orbit requires balance between two forces with opposite sign (the gravitational and centrifugal forces), and slight perturbations from the circular orbit are amplified by the effect of the Coriolis force. In the inertial frame, these numerical instabilities vanish, but the cost is that there is no centrifugal force to actively maintain the white dwarf distance, which is why it is much more likely for the orbit to prematurely decay. In either case, these results suggest at least a minimum resolution of 200 km for getting the dynamics qualitatively right. To put that into context, consider that the parameter study of Dan et al. (2014) used 40,000 SPH particles per simulation, or (for an equal mass binary) 20,000 particles per white dwarf. For, say, a  $0.9 M_{\odot} + 0.9 M_{\odot}$  white dwarf binary on a  $256^3$  zone simulation grid, there are 20,000 zones that fit within a white dwarf. We do not intend here to directly compare results between the two simulation methods. We limit ourselves to the observation that at least for grid-based codes, a parameter study such as the ones performed by Dan et al. (2012) and Dan et al. (2014) would likely not yield qualitatively convergent results if it were to use the same effective mass resolution. Instead the number of zones inside each star should at least be doubled.

## 5. PARALLEL STRATEGY AND PERFORMANCE

CASTRO is designed to be deployed on high-performance computing systems using many thousands of processors simultaneously. It is worth briefly examining our strat-

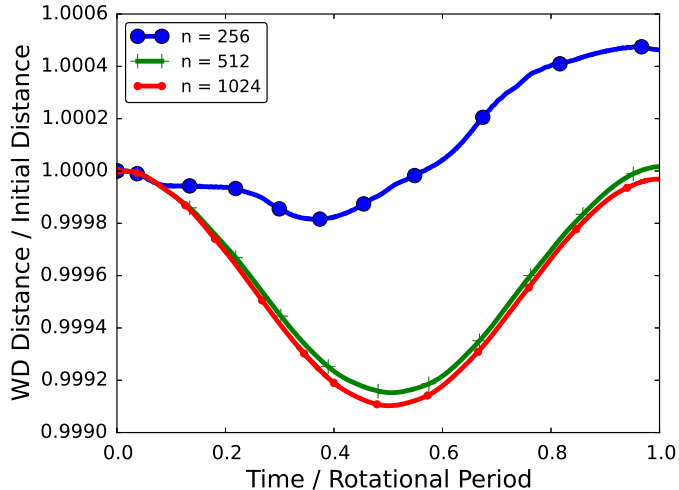


**Figure 16.** Distance between the two white dwarfs in the unequal mass system, for the first orbit. The distance is scaled by the initial orbital distance. We plot at three different resolutions, corresponding to the number of effective zones per dimension in the refined regions.

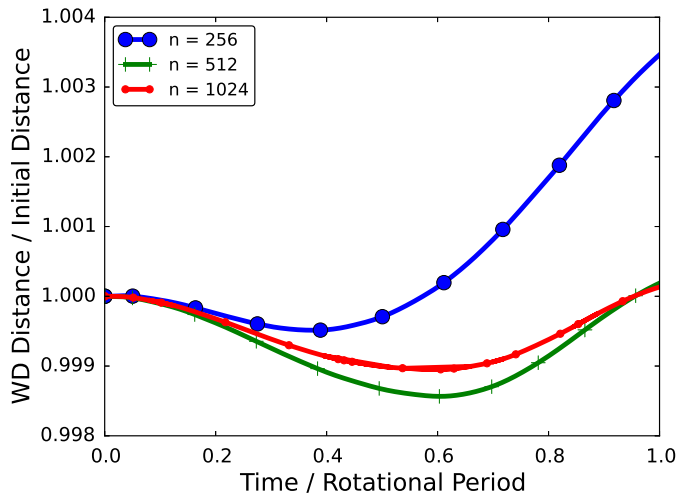


**Figure 17.** Distance between the two white dwarfs in the unequal mass system, for the first orbit. The distance is scaled by the initial orbital distance. We plot at three different resolutions, corresponding to the number of effective zones per dimension in the refined regions.

egy for parallelizing the problem over many computational nodes and our performance in situations similar to production science simulations. This is especially true because some aspects of our approach to parallelism have changed since the first *CASTRO* paper (Almgren et al. 2010), and we have obtained improved performance in certain settings.

The *BoxLib* framework that *CASTRO* is based on domain decomposes each AMR level into a number of boxes

that collectively span the level. These boxes are distributed to processors through MPI parallelism; each MPI task in general holds multiple boxes and an update includes a loop over all the boxes an MPI task owns. The distribution obeys a load-balancing algorithm that attempts to equalize the amount of work done by each processor. *BoxLib* contains a number of strategies for distributing work in this way, and by default uses a space-filling curve approach with a Morton ordering (e.g. Sasidharan & Snir (2015); Beichl & Sullivan (1998)). By experiment we have found that the most efficient load-balancing strategy for our problem is actually a simple knapsack algorithm. In this approach, the amount of work owned by a processor is proportional to the number of grid cells associated with that processor, and the algorithm attempts to ensure that all processors have a similar number of total grid cells. We demand an efficiency of 0.9, meaning that the average workload per processor should be no smaller than 90% of the maximum workload found on any processor. We find that in practice the performance is largely insensitive to this choice.

The size and shape of grid boxes is an important consideration for efficiency. Boxes that are very small suffer from a host of problems, including the larger amount of communication required between hydrodynamics solves. Additionally, the multigrid solver is less efficient if the boxes are small because there are fewer available levels for coarsening and performing V-cycles. Conversely, boxes that are too large mean that there isn’t enough work to go around when we have a large number of processors. Good performance is the result of a careful balance between these two effects. On the lower end, we require that all boxes be a multiple of 16 zones in each dimension; multigrid efficiency sharply decreases if this factor is any lower. On the upper end, we select the maximum grid size based on the number of processors we use and the total number of cells in the simulation. This size will therefore in general vary on different AMR levels. Generally we select a value in between 32 and 64 zones per dimension.

We use OpenMP to accelerate the work associated with the boxes owned by each MPI task. Originally *CASTRO* used OpenMP to accelerate individual loops in the hydrodynamics routines, such as the piecewise-parabolic edge state reconstruction and the conservative flux update. However, there is a significant amount of overhead associated with generating a new OpenMP region at each of the many different loops in a hydrodynamics algorithm. This makes such a strategy sub-optimal for use on many-core processors and GPUs. We have recently switched to a tiling approach where an OpenMP region is generated at the start of the hydrodynamics routine and the individual threads separately work on

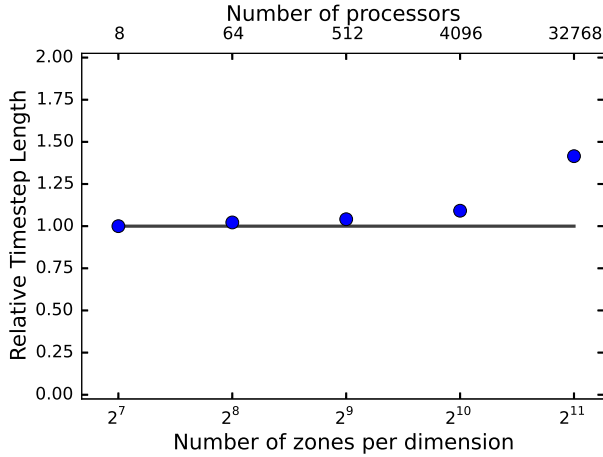


**Figure 18.** CASTRO weak scaling test, performed on Blue Waters at NCSA. Each processor had a fixed amount of work, and we increased the number of simulation zones in concert with the number of processors. The solid curve represents perfect weak scaling, while the blue circles show CASTRO’s performance at each processor count. The vertical axis measures the median time per timestep, normalized to this value for the smallest processor count.

different partitions of each box (Zhang et al. 2015). This results in much less overhead for the threading. In general we obtain more efficient simulations than could be obtained using MPI only, because there are fewer boxes and thus less communication for a given number of processor cores. We are currently developing an approach to evaluating the hydrodynamics and microphysics modules on GPUs, which will allow us to take advantage of the significant computational resources embedded in GPUs on certain systems.

To examine the parallel performance of CASTRO, we performed both strong scaling and weak scaling tests on the Blue Waters machine at the National Center for Supercomputing Applications. For the weak scaling test, whose results are shown in Figure 18, we ran a uniform grid binary white dwarf simulation for resolutions of  $128^3$  zones through  $2048^3$  zones. The number of processors was scaled with the number of zones so that each processor had the same amount of work; the smallest test used 8 processors and the largest used 32,768 (note that the number of processor cores on a Blue Waters node is twice the number of floating point units on that node). The test was run for 10 timesteps, with each timestep including two Poisson solves and a hydrodynamics update (though for a uniform grid calculation we generally do not need to perform any multigrid iterations for the first Poisson solve in a timestep, since the density distribution has not changed since the end of the last timestep). We disabled logfile and checkpoint writing, as well as calculation of diagnostic information (the latter can contribute

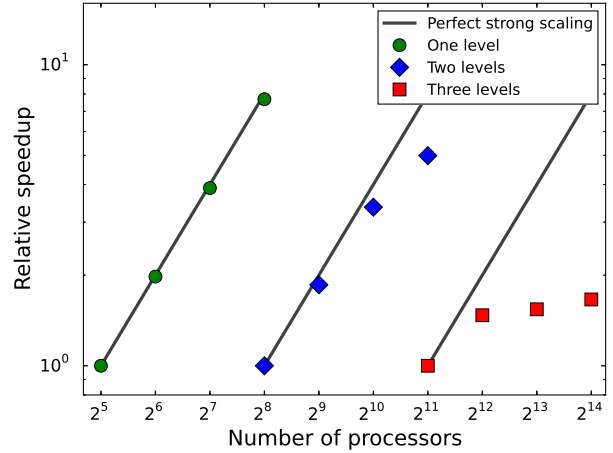


**Figure 19.** CASTRO strong scaling test performed on the Blue Waters machine at NCSA. The vertical axis measures the median time per timestep, and the horizontal axis measures the number of processors in the simulation. Data points are normalized to the time per timestep for the smallest number of processors. The green circles show the data for a simulation with one AMR level (a single uniform grid), the blue diamonds show the data for a simulation with two AMR levels (one coarse and one fine), while the red circles show the data for a test with three AMR levels (one coarse and two fine). The fine levels increase the resolution only in the regions around the stars. For each case we draw a solid curve representing perfect strong scaling.

to a significant fraction of the run time at large processor counts if computed every timestep). We computed the median wall time required per time step for each simulation, and then normalized this to the median time per timestep for the smallest simulation. We find excellent weak scaling through 4,096 processors. At the largest run, the simulation time required is slightly less than 1.5 times the amount required for the smallest simulation. This is due entirely to the increased cost of the multigrid Poisson solve in each timestep and this cannot be mitigated except by improving communication or computation efficiency in the multigrid solver. We observe that this weak scaling behavior with Poisson gravity is a significant improvement over the results presented in the first CASTRO paper.

The strong scaling test we perform uses a grid setup similar to what we use for well-resolved binary simulations. With only a uniform coarse grid, there are approximately  $2 \times 10^7$  zones. With a single refined level, we have approximately  $2 \times 10^8$  zones, typically spread over  $\sim 2000$  grids. On a second refined level, there are a similar number of zones and grids (the volume covered by this level is smaller, which offsets the greater resolution). We run a scaling test for all three cases, with the highest

processor count in each case chosen so that the number of MPI tasks is similar to the number of grids. There are no gains to be achieved from further parallelism. The results are found in Figure 19. We find excellent scaling for low to moderate numbers of processors. Parallel efficiency is well maintained when there are at least 2 grids per processor. The scaling behavior worsens at the highest processor counts, but this is an expected consequence of processors becoming work-starved. At the highest processor count in this test, there is approximately only one grid per processor. In general we find very good strong scaling behavior in the regime we are presently interested in, simulating the early phases of a simulation at moderate resolution. The strong scaling behavior is acceptable, though not perfect, at very large processor counts when self-gravity is considered.

## 6. CONCLUSIONS AND DISCUSSION

In this paper we have described the major components of a framework for simulating mergers of white dwarfs. While there is much evidence for the hypothesis that mergers (or collisions) of white dwarfs are significant contributors to the rate of Type Ia supernovae and related astronomical transients, the theoretical view of these systems is far from complete. Studying these systems over the long timescales relevant to dynamical mass transfer requires careful attention to the numerical methods used, to ensure that numerical instabilities or other errors do not unduly influence the system. Here we have described a number of common problems that may occur, including violation of the conservation of energy, a lack of hydrostatic equilibrium (at low resolution) of the stars even when not acted on by external gravitational forces, and large velocities that can be generated near the edges of stars due to the numerically sharp gradients. Some of the issues are simply unresolvable at the resolutions achievable on modern supercomputing systems; for example, it is very difficult to adequately resolve the stellar surface of a white dwarf on a three-dimensional grid, and there is justifiable room for suspicion regarding what happens there. But others are avoidable with care: energy non-conservation can be substantially mollified by using a form of the gravitational work that is explicitly conservative, and we have observed that this can be done for rotation source terms too.

We presented a set of numerical tests that show where we can and cannot trust these techniques. We spent much time considering the role of bulk motions on the grid and we conclude that there are real issues with substantial bulk velocities on static grids, that can diminish the quality of the resulting solutions to the fluid equations, but that these effects diminish with increasing resolution. We therefore make no explicit claims about the usefulness of Lagrangian versus Eulerian methods and

instead simply observe that whenever a simulation is performed, it is important to have a measure of numerical accuracy and a sense of whether we are witnessing properties that converge with increasing resolution. These problems do suggest that, where possible, we should seek to minimize bulk motions on static grids. A comparison of orbit simulations in both rotating and inertial reference frames demonstrates that in practice this is not so simple, and that a rotating reference frame has its own numerical issues for the type of simulation we desire to perform here. While decay of the stellar orbit is a commonplace feature in the inertial frame but easier to avoid in the rotating frame, the rotation forces can result in likely unphysical oscillations of the stars. It is not easy to predict the correct behavior of such systems, and therefore determine which frame is closer to being correct, though one recourse for assessing confidence in a model from a verification standpoint is to see whether the observed behavior converges with resolution. It is not clear whether at practical resolutions the results in the rotating and inertial frames will converge to each other.

Future work on this project will focus on how to build reliable equilibrium initial models of the stars and an examination of how the mass transfer episode depends on these initial conditions, and then to enable the nuclear reaction network and determine whether self-consistent thermonuclear detonations are ignited and result in events that appear similar to Type Ia supernovae. Other areas ripe for future study include: the effect of radiation on the merger process; the extent to which the result depends on the initial composition of the stars (for example, by studying the dependence of the results on the size of helium surface layers on carbon-oxygen white dwarfs, or by using white dwarf models generated by modern stellar evolution codes); and, collisions of white dwarfs. All of these are possible under the framework we have established.

The authors thank John Bell, Volker Springel, and Dominic Marcelllo for helpful discussions on gravity and hydrodynamics issues. We also thank Noel Scudder and Platon Karpov for their help with this project, especially related to visualization of the results, and Adam Jacobs for his advice on and assistance with running on supercomputing resources. Special thanks are given to the organizers of the 2015 Caltech Gravitational Wave Astrophysics School, and their supporters: the NSF under CAREER award PHY-1151197, the Sherman Fairchild Foundation, the LIGO Laboratory at Caltech, and Caltech.

This research was supported by NSF award AST-1211563. An award of computer time was provided by the Innovative and Novel Computational Impact on The-

ory and Experiment (INCITE) program. This research used resources of the Oak Ridge Leadership Computing Facility located in the Oak Ridge National Laboratory, which is supported by the Office of Science of the Department of Energy under Contract DE-AC05-00OR22725. Projects AST006 and AST106 supported use of the ORNL/Titan resource. This research is part of the Blue Waters sustained-petascale computing project, which is supported by the National Science Foundation (awards OCI-0725070 and ACI-1238993) and the state of Illinois. Blue Waters is a joint effort of the University of Illinois at Urbana-Champaign and its National Center for Supercomputing Applications. This research used resources of the National Energy Research Scientific Computing Center, which is supported by the Office of Science of the U.S. Department of Energy under Contract No. DE-AC02-05CH11231. Results in this paper were obtained using the high-performance LInx computing system at the Institute for Advanced Computational Science at Stony Brook University, which was obtained through the Empire State Development grant NYS #28451. This work used the Extreme Science and Engineering Discovery Environment (XSEDE), which is supported by National Science Foundation grant number ACI-1053575. Project AST100037 supported use of the resources NICS/Kraken and NICS/Darter.

This research has made use of NASA’s Astrophysics Data System Bibliographic Services. In addition, this research has made use of the AstroBetter blog and wiki.

*Software:* BoxLib (<https://github.com/BoxLib-Codes/BoxLib>), CASTRO (Almgren et al. (2010), <https://github.com/BoxLib-Codes/Castro>), wdmerger (<https://github.com/BoxLib-Codes/wdmerger>), GCC (<https://gcc.gnu.org/>), python (<https://www.python.org/>), matplotlib (Hunter (2007), <http://matplotlib.org/>), yt (Turk et al. (2011), <http://yt-project.org/>)

## APPENDIX

## A. CASTRO HYDRODYNAMICS CHANGES

The basic PPM algorithm in `CASTRO` has undergone a number of changes since the original code paper (Almgren et al. 2010). A discussion of the pure hydrodynamics changes along with verification of `CASTRO` when using the stellar equation of state was given in Zingale & Katz (2015). Here we discuss the changes that affect multispecies flow and source terms.

## A.1. Reference States

For all the runs, the PPM reconstruction is done using the original limiters for the parabolic profiles (Colella & Woodward 1984); see Section 2.1 for a brief discussion about the limiters. The prediction of the interface states appears as:

$$q_{i+1/2,L}^{n+1/2} = \tilde{q}_L - \sum_{\nu: \lambda_i^{(\nu)} \geq 0} l_i^{(\nu)} \cdot \left[ \tilde{q}_L - \mathcal{I}_+^{(\nu)}(q_i) \right] r_i^{(\nu)} \quad (\text{A1})$$

where  $q$  is the vector of primitive variables,  $l_i^{(\nu)}$  and  $r_i^{(\nu)}$  are the left and right eigenvectors with eigenvalue  $\lambda_i^{(\nu)}$ , with  $\nu$  the index of the characteristic wave of the system. The sum is over all the waves that result from the characteristic structure of the problem, but designed such that only waves moving toward the interface contribute to the interface value,  $q_{i+1/2,L}^{n+1/2}$ . The reference state,  $\tilde{q}_L$  is chosen to minimize the work of the characteristic projection. Finally,  $\mathcal{I}_+^{(\nu)}(q)$  is the average under the parabolic profile of quantity  $q$  of all the information that can reach the right interface of the zone  $i$  as carried by the wave  $\nu$ . The reader is referred to Miller & Colella (2002) for further details.

Since the original `CASTRO` paper, the reference state implementation has been switched to:

$$\tilde{q}_L = \begin{cases} \mathcal{I}_+^{(+)}(q_i) & \text{if } u + c > 0 \\ q_i & \text{otherwise} \end{cases} \quad (\text{A2})$$

where the (+) superscript here means the fastest wave moving to the right (the  $u + c$  eigenvalue). This is simply the average under the largest portion of the parabolic profile that could possibly reach the interface over the timestep. This is in agreement with Miller & Colella (2002) (eq. 90). The flattening in the original `CASTRO` paper has also been updated as discussed in Zingale & Katz (2015).

We comment on the choice of reference state for passively-advected quantities (like  $X_k$  or the transverse velocity), which is not typically discussed. First, consider one of the variables present in one-dimensional flow (density, velocity in the normal direction, and pressure), and let our reference state be as in Equation A2. Ignoring flattening, if there are no waves moving toward our interface, then Equation A1 reduces to:

$$q_{i+1/2,L}^{n+1/2} = \tilde{q}_L = q_i \quad (\text{A3})$$

If instead only the fastest wave is moving toward the interface, then only the term corresponding to the fastest wave in the sum will be added in Equation A1, but our choice of reference state makes that term zero by design, and our interface state is:

$$q_{i+1/2,L}^{n+1/2} = \tilde{q}_L = \mathcal{I}_+^+(q_i) \quad (\text{A4})$$

This is the desired behavior for each of these cases.

However, now consider the same approach applied to passively advected quantities. If we use the same idea of the reference state as in Equation A2, and consider a quantity  $\xi$  which should only jump across the contact, then our interface state becomes:

$$\xi_{i+1/2,L}^{n+1/2} = \tilde{\xi}_L - \underbrace{l_i^{(\circ)} \cdot \left[ \tilde{\xi}_L - \mathcal{I}_+^{(\circ)}(\xi_i) \right]}_{\text{only if } u \geq 0} r_i^{(\circ)} \quad (\text{A5})$$

Again, ignoring flattening, if  $u \geq 0$ , then we have

$$\xi_{i+1/2,L}^{n+1/2} = \tilde{\xi}_L - \left( \tilde{\xi}_L - \mathcal{I}_+^{(\circ)}(\xi_i) \right) = \mathcal{I}_+^{(\circ)}(\xi_i) \quad (\text{A6})$$

(where we used the fact that the eigenvectors are normalized to unity and don't mix in any other states when dealing with passive terms). This is the expected behavior—we see a state that is traced only by the contact wave. If  $u < 0$



but  $u + c \geq 0$ , then we instead get:

$$\xi_{i+1/2,L}^{n+1/2} = \tilde{\xi}_L = \mathcal{I}_+^{(+)}(\xi_i) \quad (\text{A7})$$

Here we used the same definition of the reference state and see that our interface state sees the profile traced under the fastest wave, not the contact. This is not the correct behavior for a passively-advected quantity.

The fix for passively-advected quantities is to simply ignore the idea of a reference state and just test on the speed of the contact itself, setting:

$$\xi_{i+1/2,L}^{n+1/2} = \begin{cases} \mathcal{I}_+^{(o)}(\xi_i) & \text{if } u > 0 \\ \xi_i & \text{otherwise} \end{cases} \quad (\text{A8})$$

### A.2. Source Term Predictor for the Hydrodynamics

In the original release of **CASTRO** we used the time-level  $n$  value of the gravitational and rotation source terms in constructing the edge-states for the hydrodynamics update. While this is formally second-order accurate, there is a better choice one can make. We have information about the trend of these source terms from previous timesteps, so we can use a predictor method to guess at a more accurate value of the gravitational and rotational fields at the  $n + 1/2$  time-level the hydro is evaluated at. Our method uses a lagged linear extrapolation. Going into the hydro update, we have both the time-level  $n$  and time-level  $n - 1$  data for  $g$  (as well as the acceleration due to rotation). From this one can construct a simple linear estimator of (say) the gravitational acceleration using a backward difference scheme at time-level  $n$ :

$$\mathbf{g}^{n+1/2} \approx \mathbf{g}^n + \frac{\Delta t_n}{2} \frac{d\mathbf{g}^n}{dt} \approx \mathbf{g}^n + \frac{\Delta t_n}{2} \left( \frac{\mathbf{g}^n - \mathbf{g}^{n-1}}{\Delta t_{n-1}} \right). \quad (\text{A9})$$

While both this method and the original method have second-order convergence properties, we have seen from testing that this new method is slightly more accurate in absolute terms. Finally, we note that this predictor is not applied in cases where we do not have a suitable time-level  $n - 1$  value of the source term, such as in the first timestep of a simulation.

We note also that we have changed slightly how we use source terms in **CASTRO**'s hydrodynamics. In the original release we would explicitly handle gravity, rotation, and user-defined external source terms separately in constructing the edge states. At present, we sum all of these source terms prior to starting the hydrodynamics update, and use a single source array with data for all components of the state. Consequently, we actually do the source-term predictor shown here on this source term array, rather than individually on each component of the forcing.

### A.3. Source Term Tracing

We note a few additional differences between the original PPM implementation of [Colella & Woodward \(1984\)](#) and **CASTRO**. In the original PPM implementation, the gravitational acceleration was reconstructed as a parabola, and this was traced under to find the forcing that affects the interface for each wave. **CASTRO** originally followed [Miller & Colella \(2002\)](#) which instead adds  $(\Delta t/2)g$  to the interface states for velocity at the end of the reconstruction. In the current implementation, we return to the original parabolic reconstruction and characteristic tracing. In fact, as described in [Section A.2](#), since we send to the hydro a single source term array that holds the sum of all the source terms (including gravity and rotation), we do the parabolic reconstruction on the full source term data. This can be controlled in **CASTRO** with the parameter `castro.ppm_trace_sources`.

For the following explanation of how the tracing works, we consider only gravity. Our system with the source appears as:

$$q_t + A(q)q_x = G \quad (\text{A10})$$

where  $G = (0, g, 0)^T$ —i.e. the gravitational source only affects  $u$ , not  $\rho$  or  $p$ . Note that in the PPM paper, they put  $G$  on the left-hand side of the primitive variable equation, so our signs are opposite. Our projections are now:

$$\sum_{\nu; \lambda^{(\nu)} \geq 0} l^{(\nu)} \cdot (\tilde{q} - \mathcal{I}_+^{(\nu)}(q) - \frac{\Delta t}{2} G) r^{(\nu)} \quad (\text{A11})$$

for the left state, and

$$\sum_{\nu; \lambda^{(\nu)} \leq 0} l^{(\nu)} \cdot (\tilde{q} - \mathcal{I}_-^{(\nu)}(q) - \frac{\Delta t}{2} G) r^{(\nu)} \quad (\text{A12})$$

for the right state. Since  $G$  is only non-zero for velocity, only the velocity changes. Writing out the sum (and performing

the vector products), we get:

$$u_{i+1/2,L}^{n+1/2} = \tilde{u}_+ - \frac{1}{2} \left[ \left( \tilde{u}_+ - \mathcal{I}_+^{(-)}(u) - \frac{\Delta t}{2} \mathcal{I}_+^{(-)}(g) \right) - \frac{\tilde{p}_+ - \mathcal{I}_+^{(-)}(p)}{C} \right] - \frac{1}{2} \left[ \left( \tilde{u}_+ - \mathcal{I}_+^{(+)}(u) - \frac{\Delta t}{2} \mathcal{I}_+^{(+)}(g) \right) + \frac{\tilde{p}_+ - \mathcal{I}_+^{(+)}(p)}{C} \right] \quad (\text{A13})$$

(The expression in the PPM paper contains  $\Delta t G$ , not  $(\Delta t/2)G$ , but we believe that the factor of 1/2 is correct. To see this, notice that if both waves are moving toward the interface, then the source term that is added to the interface state is  $(\Delta t/4)(\mathcal{I}_+^{(-)}(g) + \mathcal{I}_+^{(+)}(g))$  for the left state, which reduces to  $(\Delta t/2)g$  for constant  $g$ —this matches the result from Taylor expanding to the interface at the half-time (as in [Miller & Colella 2002](#)).)

There is one additional effect of this change—now the gravitational source is seen by all Riemann solves (including the transverse solves) whereas previously it was only added to the final unsplit interface states. Both methods are second-order accurate.

## B. PROOF OF ENERGY CONSERVATION IN SIMULATIONS USING SELF-GRAVITY

In [Section 2.3.1](#), we described our approach to updating the gas energy in response to motions of fluid through the self-generated gravitational potential using [Equation 11](#). While it is straightforward to observe that this approach should be conservative for an arbitrary fixed external potential  $\Phi$ , it is not as obvious that this should be so for a self-generated potential which changes in response to mass motions on the domain. To see that this still holds for the self-generated gravitational potential  $\Phi$ , let us start with [Equation 11](#) in a slightly revised form:

$$\Delta(\rho E)_i = -\frac{1}{2} \sum_j \Delta\rho_{ij} (\Phi_i - \Phi_j) \quad (\text{B1})$$

where by  $\Delta\rho_{ij}$  we mean the density transferred from zone  $j$  to zone  $i$ , so that  $\Delta\rho_{ij} = -\Delta\rho_{ji}$ , and the sum is over all zone indices  $j$  that are adjacent to zone  $i$ . Let us define  $\Phi_{ij} = \Phi_{ji} = (\Phi_i + \Phi_j)/2$  as the potential on the zone interface between zones  $i$  and  $j$ . Then we have:

$$\Delta(\rho E)_i = - \sum_j \Delta\rho_{ij} (\Phi_i - \Phi_{ij}). \quad (\text{B2})$$

We can evaluate the sum for all of the terms proportional to  $\Phi_i$  by observing that the change in density from time-level  $n$  to time-level  $n+1$  is the sum of the density fluxes from all adjacent zones.

$$\Delta(\rho E)_i = -(\rho_i^{n+1} - \rho_i^n) \Phi_i + \sum_j \Delta\rho_{ij} \Phi_{ij}$$

Now let us sum this over all zones  $i$  in the domain, and ignore the domain boundaries, or assume that they are far enough away from the region of compact support for  $\rho$  that  $\Phi$  is negligible there. As the second term on the right-hand side is antisymmetric in  $i$  and  $j$ , it cancels when summing adjacent zones, and we have:

$$\sum_i (\rho E)_i^{n+1} - \sum_i (\rho E)_i^n = -\frac{1}{2} \sum_i (\Phi_i^{n+1} + \Phi_i^n) (\rho_i^{n+1} - \rho_i^n)$$

Note that, as explained the text, we are using a time-centered  $\Phi$  to correspond to the mass fluxes at time-level  $n+1/2$ . Finally we re-write this in a form where the difference in total energy between time-levels  $n$  and  $n+1$  is on the left-hand side and any sources causing this to be non-zero are on the right-hand side:

$$\begin{aligned} \sum_i \left( \rho E + \frac{1}{2} \rho \Phi \right)_i^{n+1} - \sum_i \left( \rho E + \frac{1}{2} \rho \Phi \right)_i^n &= \frac{1}{2} \sum_i (\Phi_i^{n+1} \rho_i^n - \Phi_i^n \rho_i^{n+1}) \\ &= \frac{1}{8\pi G} \sum_i (\Phi_i^{n+1} \nabla^2 \Phi_i^n - \Phi_i^n \nabla^2 \Phi_i^{n+1}) \end{aligned} \quad (\text{B3})$$

[Equation B3](#) expresses total energy conservation if and only if the right-hand side vanishes. We observe that the right-hand side has the form of a variant of the divergence theorem often called Green's second identity:

$$\int (\Phi^n \nabla^2 \Phi^{n+1} - \Phi^{n+1} \nabla^2 \Phi^n) dV = \int (\Phi^n \nabla \Phi^{n+1} - \Phi^{n+1} \nabla \Phi^n) \cdot d\mathbf{S}, \quad (\text{B4})$$

where  $d\mathbf{S}$  is the area element with vector component parallel to the outward normal. The analogous result holds for the discretized form in [Equation B3](#). With the assumptions used above, the right-hand side of [Equation B4](#) will vanish as the surface integral is evaluated at infinity, where the potential tends to zero. This concludes the proof that the method is conservative when the potential used at the zone interfaces is time-centered, even in light of the change of the potential over the timestep due to the mass motion that is causing the change in the energy.

From the above discussion it is straightforward to see exactly why the method is not fully conservative to machine precision in practice. First, we cannot simulate the domain out to infinity, so Green's second identity does not hold exactly and there is some loss or addition of energy at domain boundaries. Second, [Equation B3](#) holds in the continuum limit by using the Poisson equation, but in practice it is not exactly true that  $\rho_i = 4\pi G \nabla^2 \Phi_i$  due to small errors in the potential at the level of the tolerances used in the Poisson solver.

### C. FORMULATION OF THE MULTIPOLE EXPANSION FOR THE GRAVITATIONAL POTENTIAL

The integral formulation of the gravitational potential, using a series expansion in spherical harmonics, is:

$$\Phi(\mathbf{x}) = -G \sum_{l=0}^{\infty} \sum_{m=-l}^l \frac{4\pi}{2l+1} \int \rho(\mathbf{x}') Y_{lm}(\theta, \phi) Y_{lm}^*(\theta', \phi') \frac{r_{<}^l}{r_{>}^{l+1}} dV', \quad (\text{C1})$$

where  $\theta$  is the polar angle and  $\phi$  is the azimuthal angle,  $r \equiv |\mathbf{x}|$  is the radial distance, and at any point in the domain  $r_{<}$  is the smaller of  $r$  and  $r'$ , and  $r_{>}$  is the larger of the two. This immediately suggests writing the potential at any location as the sum of two series:

$$\Phi(\mathbf{x}) = -G \sum_{l=0}^{\infty} \sum_{m=-l}^l \frac{4\pi}{2l+1} [q_{lm}^L(\mathbf{x}) r^{-l-1} + q_{lm}^U(\mathbf{x}) r^{-l-1}] Y_{lm}(\theta, \phi),$$

where we have defined two multipole moments as integrals over the domain:

$$q_{lm}^L(\mathbf{x}) = \int dV' \rho(\mathbf{x}') Y_{lm}^*(\theta', \phi') \Theta(r - r') r'^l \quad (\text{C2})$$

$$q_{lm}^U(\mathbf{x}) = \int dV' \rho(\mathbf{x}') Y_{lm}^*(\theta', \phi') \Theta(r' - r) r'^{-l-1}. \quad (\text{C3})$$

$\Theta(r)$  is the standard step function, equal to one if the argument is positive and zero if the argument is negative. Geometrically,  $q^L(\mathbf{x})$  is an integral containing only mass interior to  $|\mathbf{x}|$ , and  $q^U(\mathbf{x})$  is an integral containing only mass exterior to  $|\mathbf{x}|$ . Provided that one has computed these two integrals for a point  $\mathbf{x}$ , one can use the series expansion to calculate the potential at that point in principle to arbitrary accuracy by including higher order terms.

We prefer to work with solely real-valued quantities, and so we make use of the addition theorem for spherical harmonics ([Jackson 1998](#), Section 3.6):

$$\begin{aligned} \frac{4\pi}{2l+1} \sum_{m=-l}^l Y_{lm}^*(\theta', \phi') Y_{lm}(\theta, \phi) &= P_l(\cos \theta) P_l(\cos \theta') \\ &+ 2 \sum_{m=1}^l \frac{(l-m)!}{(l+m)!} P_l^m(\cos \theta) P_l^m(\cos \theta') [\cos(m\phi) \cos(m\phi') + \sin(m\phi) \sin(m\phi')]. \end{aligned} \quad (\text{C4})$$

The  $P_l(x)$  are the Legendre polynomials and the  $P_l^m(x)$  are the associated Legendre polynomials. We construct them using a stable recurrence relation given known values for  $l = 0$  and  $l = 1$ . We can then formulate the expansion in a different way:

$$\begin{aligned} \Phi(\mathbf{x}) &= -G \sum_{l=0}^{\infty} \left\{ Q_l^{(L,0)}(\mathbf{x}) P_l(\cos \theta) r^{-l-1} + Q_l^{(U,0)}(\mathbf{x}) P_l(\cos \theta) r^l \right. \\ &+ \sum_{m=1}^l \left[ Q_{lm}^{(L,C)}(\mathbf{x}) \cos(m\phi) + Q_{lm}^{(L,S)}(\mathbf{x}) \sin(m\phi) \right] P_l^m(\cos \theta) r^{-l-1} \\ &\left. + \sum_{m=1}^l \left[ Q_{lm}^{(U,C)}(\mathbf{x}) \cos(m\phi) + Q_{lm}^{(U,S)}(\mathbf{x}) \sin(m\phi) \right] P_l^m(\cos \theta) r^l \right\} \end{aligned} \quad (\text{C5})$$

The multipole moments now take the form:

$$Q_l^{(L,0)}(\mathbf{x}) = \int P_l(\cos \theta') \Theta(r - r') r'^l \rho(\mathbf{x}') d^3 x' \quad (\text{C6})$$

$$Q_l^{(U,0)}(\mathbf{x}) = \int P_l(\cos \theta') \Theta(r' - r) r'^l \rho(\mathbf{x}') d^3 x' \quad (\text{C7})$$

$$Q_{lm}^{(L,C)} = 2 \frac{(l-m)!}{(l+m)!} \int P_l^m(\cos \theta') \cos(m\phi') \Theta(r - r') r'^l \rho(\mathbf{x}') d^3 x' \quad (\text{C8})$$

$$Q_{lm}^{(U,C)} = 2 \frac{(l-m)!}{(l+m)!} \int P_l^m(\cos \theta') \cos(m\phi') \Theta(r' - r) r'^{l-1} \rho(\mathbf{x}') d^3 x' \quad (\text{C9})$$

$$Q_{lm}^{(L,S)} = 2 \frac{(l-m)!}{(l+m)!} \int P_l^m(\cos \theta') \sin(m\phi') \Theta(r - r') r'^l \rho(\mathbf{x}') d^3 x' \quad (\text{C10})$$

$$Q_{lm}^{(U,S)} = 2 \frac{(l-m)!}{(l+m)!} \int P_l^m(\cos \theta') \sin(m\phi') \Theta(r' - r) r'^{l-1} \rho(\mathbf{x}') d^3 x'. \quad (\text{C11})$$

In practice, of course, we select some maximum value  $l_{\max}$  at which we terminate the summation, determined either by computational efficiency requirements or by the fact that there is little information at high orders for sufficiently smooth mass distributions. In **CASTRO** we have the capability to compute any of the above multipole moments, though in this paper we are only using the multipole expansion to calculate the boundary conditions on the potential, and so we neglect calculation of the moments with a  $U$  subscript as we are assuming that all of the mass is interior to the boundary. [Equation 14](#) is directly recovered under these conditions.

## REFERENCES

- Agertz, O., Moore, B., Stadel, J., et al. 2007, *MNRAS*, 380, 963 [1](#)
- Almgren, A. S., Bell, J. B., Nonaka, A., & Zingale, M. 2008, *ApJ*, 684, 449 [3.2](#)
- Almgren, A. S., Beckner, V. E., Bell, J. B., et al. 2010, *ApJ*, 715, 1221 [2](#), [2.3](#), [4](#), [5](#), [6](#), [A](#)
- Amaro-Seoane, P., Aoudia, S., Babak, S., et al. 2013, *GW Notes*, Vol. 6, p. 4-110, 6, 4 [3.3.1](#)
- Beichl, I., & Sullivan, F. 1998, *Computational Science Engineering*, IEEE, 5, 92 [5](#)
- Benz, W., Cameron, A. G. W., Press, W. H., & Bowers, R. L. 1990, *ApJ*, 348, 647 [1](#)
- Blanchet, L., Damour, T., & Schaefer, G. 1990, *MNRAS*, 242, 289 [3.3.1](#), [3.3.1](#)
- Byerly, Z. D., Adelstein-Lelbach, B., Tohline, J. E., & Marcello, D. C. 2014, *ApJS*, 212, 23 [2.4](#)
- Colella, P., & Sekora, M. D. 2008, *Journal of Computational Physics*, 227, 7069 [2.1](#)
- Colella, P., & Woodward, P. R. 1984, *Journal of Computational Physics*, 54, 174 [2.1](#), [A.1](#), [A.3](#)
- Dan, M., Rosswog, S., Brüggem, M., & Podsiadlowski, P. 2014, *MNRAS*, 438, 14 [1](#), [4.4](#)
- Dan, M., Rosswog, S., Guillochon, J., & Ramirez-Ruiz, E. 2011, *ApJ*, 737, 89 [1](#), [3.2](#)
- . 2012, *MNRAS*, 422, 2417 [1](#), [3.1](#), [4.4](#)
- D’Souza, M. C. R., Motl, P. M., Tohline, J. E., & Frank, J. 2006, *ApJ*, 643, 381 [1](#)
- Eggleton, P. P. 1983, *ApJ*, 268, 368 [3.2](#)
- Fryer, C., Benz, W., Herant, M., & Colgate, S. A. 1999, *ApJ*, 516, 892 [1](#)
- Fryer, C. L., & Diehl, S. 2008, in *Astronomical Society of the Pacific Conference Series*, Vol. 391, *Hydrogen-Deficient Stars*, ed. A. Werner & T. Rauch, 335 [1](#)
- Guerrero, J., García-Berro, E., & Isern, J. 2004, 413, 257 [1](#)
- Guillochon, J., Dan, M., Ramirez-Ruiz, E., & Rosswog, S. 2010, *ApJL*, 709, L64 [1](#), [4.3](#)
- Hillebrandt, W., Kromer, M., Röpke, F. K., & Ruiter, A. J. 2013, *Frontiers of Physics*, 8, 116 [1](#)
- Hillebrandt, W., & Niemeyer, J. C. 2000, *Annu. Rev. Astron. Astrophys.*, 38, 191 [1](#)
- Hopkins, P. F. 2015, *MNRAS*, 450, 53 [4.3.1](#)
- Hoyle, F., & Fowler, W. A. 1960, *ApJ*, 132, 565 [1](#)
- Hummer, G. 1996, *Journal of Electrostatics*, 36, 285 [2.3.3](#)
- Hunter, J. D. 2007, *Computing In Science & Engineering*, 9, 90 [3](#), [6](#)
- Iben, Jr., I., & Tutukov, A. V. 1984, *ApJS*, 54, 335 [1](#)
- Jackson, J. D. 1998, *Classical Electrodynamics*, 3rd Edition [C](#)
- Jiang, Y.-F., Belyaev, M., Goodman, J., & Stone, J. M. 2013, *New A*, 19, 48 [2.3.1](#), [2.3.1](#)
- Kashyap, R., Fisher, R., García-Berro, E., et al. 2015, *ApJL*, 800, L7 [1](#)
- Livio, M. 2000, in *Type Ia Supernovae, Theory and Cosmology*, ed. J. C. Niemeyer & J. W. Truran, 33 [1](#)
- Lorén-Aguilar, P., Guerrero, J., Isern, J., Lobo, J. A., & García-Berro, E. 2005, *MNRAS*, 356, 627 [3.3.1](#)
- Lorén-Aguilar, P., Isern, J., & García-Berro, E. 2009, 500, 1193 [1](#)
- MacMillan, W. 1958, *The theory of the potential*, Dover books on physics and mathematical physics (Dover Publications), 72–79 [2.3.3](#)
- Malone, C. M., Nonaka, A., Woosley, S. E., et al. 2014, *ApJ*, 782, 11 [2.3.2](#)
- Maoz, D., Mannucci, F., & Nelemans, G. 2014, *ARA&A*, 52, 107 [1](#)
- Marcello, D. C., & Tohline, J. E. 2012, *ApJS*, 199, 35 [2.4](#), [4.4](#)
- McNally, C. P., Lyra, W., & Passy, J.-C. 2012, *ApJS*, 201, 18 [4.3.1](#), [4.3.1](#)
- Miller, G. H., & Colella, P. 2002, *Journal of Computational Physics*, 183, 26 [2.1](#), [A.1](#), [A.1](#), [A.3](#), [A.3](#)
- Mochkovitch, R., & Livio, M. 1990, *A&A*, 236, 378 [1](#)
- Moll, R., Raskin, C., Kasen, D., & Woosley, S. E. 2014, *ApJ*, 785, 105 [1](#)
- Motl, P. M., Frank, J., Tohline, J. E., & D’Souza, M. C. R. 2007, *ApJ*, 670, 1314 [1](#)
- Motl, P. M., Tohline, J. E., & Frank, J. 2002, *ApJS*, 138, 121 [1](#), [2.4](#), [3.2](#)
- Nomoto, K., & Iben, Jr., I. 1985, *ApJ*, 297, 531 [1](#)
- Pakmor, R., Edelmann, P., Röpke, F. K., & Hillebrandt, W. 2012a, *MNRAS*, 424, 2222 [3.2](#)
- Pakmor, R., Hachinger, S., Röpke, F. K., & Hillebrandt, W. 2011, *A&A*, A117 [1](#)
- Pakmor, R., Kromer, M., Röpke, F. K., et al. 2010, *Nature*, 463, 61 [1](#)
- Pakmor, R., Kromer, M., Taubenberger, S., et al. 2012b, *ApJL*, 747, L10 [1](#)
- Pakmor, R., Kromer, M., Taubenberger, S., & Springel, V. 2013, *ApJL*, 770, L8 [1](#)
- Perlmutter, S., Aldering, G., Goldhaber, G., et al. 1999, *ApJ*, 517, 565 [1](#)
- Price, D. J. 2008, *Journal of Computational Physics*, 227, 10040 [1](#)
- Rasio, F. A., & Shapiro, S. L. 1995, *ApJ*, 438, 887 [1](#)
- Raskin, C., Scannapieco, E., Fryer, C., Rockefeller, G., & Timmes, F. X. 2012, *ApJ*, 746, 62 [1](#)
- Rendleman, C. A., Beckner, V. E., Lijewski, M., Crutchfield, W., & Bell, J. B. 2000, *Computing and Visualization in Science*, 3, 147 [2](#)
- Riess, A. G., Filippenko, A. V., Challis, P., et al. 1998, 116, 1009 [1](#)
- Robertson, B. E., Kravtsov, A. V., Gnedin, N. Y., Abel, T., & Rudd, D. H. 2010, *MNRAS*, 401, 2463 [4.3](#), [4.3.1](#), [4.3.1](#)
- Rosswog, S., Speith, R., & Wynn, G. A. 2004, *MNRAS*, 351, 1121 [3.2](#)
- Saio, H., & Nomoto, K. 1985, 150, L21 [1](#)
- Sasidharan, A., & Snir, M. 2015 [5](#)
- Sato, Y., Nakasato, N., Tanikawa, A., et al. 2015, *ApJ*, 807, 105 [1](#)
- Schwab, J., Shen, K. J., Quataert, E., Dan, M., & Rosswog, S. 2012, *MNRAS*, 427, 190 [1](#)
- Segretain, L., Chabrier, G., & Mochkovitch, R. 1997, *ApJ*, 481, 355 [1](#)
- Shen, K. J., Bildsten, L., Kasen, D., & Quataert, E. 2012, *ApJ*, 748, 35 [1](#)
- Shu, F. H. 1992, *The physics of astrophysics. Volume II: Gas dynamics.* [2.3.1](#)
- Springel, V. 2010, *MNRAS*, 401, 791 [2.3.1](#), [2.3.1](#), [4.3](#)
- Swesty, F. D., Wang, E. Y. M., & Calder, A. C. 2000, *ApJ*, 541, 937 [2.4](#), [3.2](#), [4.4](#)
- Tanikawa, A., Nakasato, N., Sato, Y., et al. 2015, *ApJ*, 807, 40 [1](#)
- Tasker, E. J., Brunino, R., Mitchell, N. L., et al. 2008, *MNRAS*, 390, 1267 [4.3](#), [4.3.2](#)
- Timmes, F. X., & Swesty, F. D. 2000, *ApJS*, 126, 501 [2.2](#)
- Turk, M. J., Smith, B. D., Oishi, J. S., et al. 2011, *ApJS*, 192, 9 [3](#), [6](#)
- Tutukov, A. V., & Yungelson, L. R. 1979, *Acta Astron.*, 29, 665 [1](#)
- van Kerkwijk, M. H., Chang, P., & Justham, S. 2010, *ApJL*, 722, L157 [1](#)
- Wadsley, J. W., Veeravalli, G., & Couchman, H. M. P. 2008, *MNRAS*, 387, 427 [4.3](#)
- Waldvogel, J. 1976, *Zeitschrift für angewandte Mathematik und Physik ZAMP*, 27, 867 [2.3.3](#)
- Webbink, R. F. 1984, *ApJ*, 277, 355 [1](#)
- Whelan, J., & Iben, Jr., I. 1973, *ApJ*, 186, 1007 [1](#)
- Yoon, S., Podsiadlowski, P., & Rosswog, S. 2007, *MNRAS*, 380, 933 [1](#)

Zhang, W., Almgren, A., Day, M., et al. 2015, SIAM Journal on Scientific Computing, submitted [5](#)

Zhu, C., Chang, P., van Kerkwijk, M. H., & Wadsley, J. 2013, ApJ, 767, 164 [1](#)

Zhu, Q., Hernquist, L., & Li, Y. 2014, ArXiv e-prints, arXiv:[arXiv:1410.4222](#) [1](#)

Zingale, M., & Katz, M. P. 2015, ApJS, 216, 31 [A](#), [A.1](#)

Zingale, M., Dursi, L. J., ZuHone, J., et al. 2002, ApJS, 143, 539 [4.1](#)